Structural and biochemical insights into heterotetramer formation between human oncogenic K-Ras4B^{G12V} and Rgl2, a RalA/B activator

Mishal Tariq[1], Teppei Ikeya[2], Naoyuki Togashi[2], Louise Fairall[1,3], Carlos Bueno-Alejo[3], Syun Kamei[2], Beatriz Romartinez-Alonso[1,3], Miguel Angel Muro Campillo[1], Andrew J. Hudson[3,4], Yutaka Ito[2], John W.R. Schwabe[1,3], Cyril Dominguez[1,3], and Kayoko Tanaka[1]

1. Department of Molecular and Cell Biology, University of Leicester
2. Department of Chemistry, Tokyo Metropolitan University
3. Leicester Institute of Structure and Chemical Biology, University of Leicester
4. Department of Chemistry, University of Leicester

*Paste corresponding author name(s) here.

*Kayoko Tanaka

Email: kt96@le.ac.uk

Author Contributions: M.T., T.I., Y.I., C.D. and K.T. designed research. M.T., T.I., N.T., C.B.-A., S.K., M.A.M.C., C.D. and K.T. performed research. M.T., T.I., N.T., L.F., C.B.-A., S.K., B.R.-A, A.J.H., Y.I., J.W.R.S., C.D. and K.T. analyzed data. M.T., T.I., C.D. and K.T. wrote the manuscript with feedback from all the authors.

Competing Interest Statement: The authors declare that they have no conflicts of interest with the contents of this work.

Classification: Biochemistry

Keywords: Ras signaling, RalA/B pathway, Structural Biology

Abstract

Ras is a small GTPase that regulates fundamental cellular activities. Activated Ras transduces the signalling by directly interacting with effector proteins. About a quarter of total human cancers carry mutations in Ras isoforms, and hence understanding the structure and molecular interactions of Ras with effector proteins is of vital importance. Accumulating evidence suggests that small GTPases, RalA and RalB, and their activators, Ral guanine nucleotide exchange factors (RalGEFs), play an essential role in oncogenic Ras-induced signalling. We, therefore, studied the interaction between human K-Ras4B and the Ras binding domain (RBD) of Rgl2 ($Rgl2^{RBD}$) because, among RBD-containing RalGEFs, Rgl2 is predicted to be most significantly in complex with Ras in over 29 human tissues [Catozzi S, Halasz M, & Kiel C (2021) Predicted 'wiring landscape' of Ras-effector interactions in 29 human tissues. *NPJ Syst Biol Appl* 7(1):10]. We show that the affinity between K-Ras4B and $Rgl2^{RBD}$ is increased when K-Ras4B carries oncogenic mutation G12V. The crystal structure of the K-$Ras4B^{G12V}$: $Rgl2^{RBD}$ complex shows that a heterotetramer is formed where the Switch I and Switch II regions of a single K-Ras^{G12V} molecule interact with two separate $Rgl2^{RBD}$. This structural arrangement is highly similar to the H-Ras^{E31K}:RALGDS crystal structure and is distinct from the well-characterised Ras:RAF^{RBD} complexes. Importantly, the G12V mutation was found at the dimer interface of K-$Ras4B^{G12V}$ with its partner. Solution state NMR and mass photometry analyses support the heterotetramer formation in solution. Our study reveals a distinct mode of Ras:effector complex formation by RalGEFs, and points to a possibility that K-$Ras4B^{G12V}$ oncogenicity originates from the formation of a stable complex with Rgl2.

Significance Statement

The best-characterised Ras:effector interaction is the Ras:Raf1 kinase complex that leads to ERK activation. However, accumulating evidence suggests that oncogenic Ras signalling does not always hyperactivate ERK and Akt pathways, and the less-studied RalA/B pathway may be a key player in oncogenic-Ras induced tumorigenesis. In this work, we report that the G12V oncogenic K-Ras4B mutation substantially increases the affinity with the Ras associating (RA) domain of Rgl2, an activator of RalA/B. The K-$Ras4B^{G12V}$:$Rgl2^{RA}$ complex forms a heterotetramer, with the oncogenic mutant residue located directly at the K-$Ras4B^{G12V}$: K-$Ras4B^{G12V}$ interface. The binding mode is structurally distinct from other Ras:effector complexes, offering a possible mechanistic explanation for how the oncogenic K-$Ras4B^{G12V}$ hyperactivates the RalA/B pathway.

Main Text

Introduction

Ras belongs to a family of small G protein that switches between two states, GDP-bound form (Ras^{GDP}) and GTP-bound form (Ras^{GTP}), and regulates a wide range of cellular activities (1). Guanine nucleotide exchange factors (GEFs), typically activated by growth factor signalling, mediate the conversion of Ras^{GDP} to Ras^{GTP}, whilst the GTP-bound status lasts only transiently as the intrinsic GTPase activity, aided by the GTPase activating Proteins (GAPs), hydrolyses the bound GTP into GDP (2). Ras acts as a signalling hub where the Ras^{GTP}, but not Ras^{GDP}, physically interacts with multiple Ras effectors, which then transmit the signal to downstream molecules, including ERK, Akt and small G proteins RalA and RalB (3).

There are three human *RAS* genes, *K-RAS*, *N-RAS* and *H-RAS*, and as *K-RAS* is alternatively spliced at exon 4, the three *RAS* genes produce four Ras isoforms K-Ras4A, K-Ras4B, N-Ras and H-Ras (4). Among them, *K-RAS4B* typically represents more than half of all *RAS* transcripts (5). The Catalogue Of Somatic Mutations In Cancer (COSMIC) shows that about 25% of all cancers carry mutations in *RAS* genes, and *K-RAS* is responsible for about 70% of these mutations (COSMIC, v.95). Hence, it is vital to obtain more insights into how the oncogenic K-Ras signalling leads to cancers.

Extensive earlier biochemical studies revealed that oncogenic *RAS* mutations cause a reduction of the GTP hydrolysis rate, generating an increased population of Ras^{GTP} (6-11). This likely leads to an overactivation of the downstream signalling pathways and therefore is considered the major cause of the K-Ras oncogenicity. In addition, recent biochemical, structural and molecular modelling studies indicate that oncogenic *RAS* mutations affect the interaction kinetics with the effector molecules and may trigger a biased overactivation of a set of effectors (12-15). Therefore, obtaining more insights into the Ras-effector interaction mechanism is essential to understanding the oncogenic-Ras mediated tumorigenesis process.

Among Ras effectors, Raf kinase and PI3K, which ignite ERK and Akt signalling respectively, have attracted much attention, especially because they were found not only to be activated by oncogenic Ras but also to be able to carry oncogenic mutations themselves (16, 17). However, accumulating evidence suggests that the misregulation of Ral GTPases, RalA and RalB, rather

than ERK and Akt signalling pathways, may be the initial trigger of oncogenic-Ras induced tumorigenesis. For example, in the oncogenic K-ras(G12D) knock-in mouse model, although neoplastic and developmental defects were observed, hyper-activation of ERK or Akt was undetected (18). In humans, ERK hyper-activation is often missing in cancer cell lines and tissues with oncogenic Ras mutations, whereas RalA and RalB are essential in oncogenic-Ras induced cell proliferation, motility and tumorigenesis (19-26). Therefore, a biased misregulation of the Ral GTPases may be the critical feature behind Ras oncogenicity. Indeed, NMR-based effector competition assays suggested the intriguing possibility that the oncogenic Ras molecules may develop an altered effector preference leading to a biased hyperactivation of RalA (12).

Activation of RalA and RalB is mediated by guanine nucleotide exchange factors (RalGEFs). There are eight RalGEFs reported for humans, and four of them, RALGDS, Rgl1, Rgl2 and Rgl3, have a Ras-association (RA) domain (in this work, we generically call it Ras Binding Domain (RBD)) responsible for Ras-binding (27). RALGDS was the first to be identified as a Ras effector among these RalGEFs and is by far the most studied (28). RALGDS is one of the first effector molecules that was crystallised together with an active Ras. Rat RALGDS was co-crystalised with human H-Ras harbouring an E31K mutation, which helped complex formation (29). A recent modelling approach, integrating proteomic data of Ras, its 56 effectors and their interaction affinities, predicts that Rgl2 would generate the highest concentration of Ras:effector complex among RalGEFs in 28 out of 29 healthy human tissues (30). Furthermore, a critical contribution of Rgl2 in oncogenic Ras induced tumour phenotypes has been reported (31). However, the Ras:Rgl2 complex interface has not been studied.

In this report, we examined the mode of interaction between human K-Ras4B and the RBD of Rgl2 ($Rgl2^{RBD}$). We observed striking affinity increase of the interaction of K-Ras4B with the$Rgl2^{RBD}$ upon introduction of G12V oncogenic mutation. Our crystal structure of K-$Ras4B^{G12V}$:$Rgl2^{RBD}$ complex shows a heterotetramer formation, highly similar to the reported H-Ras^{E31K}:$RALGDS^{RBD}$ complex, but distinct from other Ras:effector complexes including Ras:Raf1 kinase. Strikingly, the G12V oncogenic mutation is located at the dimer interface of K-$Ras4B^{G12V}$ with its homodimeric partner. Solution NMR analyses support the heterotetramer formation and mass photometry confirms the presence of the heterotetramer. Our findings provide an

interesting possibility that K-Ras4B^{G12V} oncogenicity might be due to its capability to form a heterotetramer with Rgl2.

Results

Active K-Ras4B^{G12V} has a stronger affinity to Rgl2^{RBD} than K-Ras4B^{WT}

Throughout this study, we used recombinant bacteria constructs of human K-Ras4B lacking the C-terminal hyper-variable region and the Rgl2 RBD (Rgl2^{RBD}) consisting of amino acids 648 – 735 of human Rgl2. The binding of Rgl2^{RBD} and K-Ras4B^{G12V} was confirmed for the active K-Ras4B^{G12V} loaded with a non-hydrolysable GTP analogue (Guanosine-5'-[(β,γ)-imido]triphosphate (GMPPNP)), by GST-pulldown assays (Supplementary Fig. S1A and S1B). To examine whether the binding mode of Rgl2^{RBD} differs between K-Ras4B^{WT} and K-Ras4B^{G12V}, the binding affinities were determined by biolayer interferometry (BLI). We noticed that both K-Ras4B^{WT} and K-Ras4B^{G12V}, purified at 4°C at all times as described in the Materials and Methods, retained GTP as the major bound guanine nucleotide, and we confirmed that the K-Ras4B^{WT} and K-Ras4B^{G12V} samples that were subjected to the incubation condition of the BLI assay were still associated with GTP (Fig. 1A). Therefore, we used these GTP-bound samples without loading GMPPNP so that we could minimize possible artefacts caused by GMPPNP. The on/off kinetics between K-Ras4B and Rgl2 were fast for both wildtype and G12V mutant (Fig. 1B lower panels), and the sensorgram curves could not be fitted to the pre-programmed curve fitting models (Data Analysis HT Software, Sartorius). Therefore, we deduced the equilibrium dissociation constant (K_D) using steady-state analysis (Fig. 1B upper panels). Strikingly, the affinity between Rgl2^{RBD} and K-Ras4B was substantially increased when K-Ras4B carried an oncogenic mutation, G12V, where Glycine at position 12 is replaced with Valine. The circular dichroic (CD) spectra for K-Ras4B^{WT} and K-Ras4B^{G12V} samples across the increasing temperature from 20°C to 90°C also showed improved structural stability for K-Ras4B^{G12V}, which might contribute to the higher affinity towards Rgl2^{RBD} (Fig. 1 C-E).

A 2:2 tetramer of K-Ras4B^{G12V}:Rgl2^{RBD} complex in the crystal structure

We conducted crystallization trials to obtain structural insights into the K-Ras4B:Rgl2^{RBD} complex. To purify the complex, a mixture of K-Ras4B and Rgl2^{RBD} was loaded onto a size-exclusion column. We could obtain the K-Ras4B^{G12V}:Rgl2^{RBD} complex in a peak that eluted earlier

than K-Ras4B^{G12V} alone (Supplementary Fig. S1C). However, we were unable to obtain an elution peak for K-Ras4B^{WT}:Rgl2^{RBD} complex (Supplementary Fig. S1D). The inability of K-Ras4B^{WT} to form a stable complex that survives the gel filtration chromatography is consistent with the relatively low affinity between K-Ras4B^{WT} and Rgl2^{RBD} seen in Fig. 1B.

Crystals of the K-Ras4B^{G12V}:Rgl2^{RBD} complex were obtained which diffracted at a resolution of 3.07Å (Table 1). After molecular replacement with the structure of the human H-Ras^{E31K}:rat RALGDS^{RBD} complex (PDB ID 1LFD) (29), the K-Ras4B^{G12V}:Rgl2^{RBD} structure was manually built using Coot (32) and was refined with PHENIX (33)(Fig. 2A). The overall arrangement of K-Ras4B^{G12V}:Rgl2^{RBD} crystal structure is similar to H-Ras^{E31K}:RALGDS^{RBD} crystal structure (PDB ID 1LFD (29))(Supplementary Fig. S2A). The complex forms a 2:2 heterotetramer where β2 (within Switch I) of Ras and β2 of Rgl2^{RBD} generate a continuously extended β-sheet, along with interaction at Switch II of the same Ras molecule with the second Rgl2^{RBD} (Fig. 2B, Supplementary Fig. S3A). In both K-Ras4B^{G12V}:Rgl2^{RBD} and H-Ras^{E31K}:RALGDS^{RBD} cases, the Ras-Ras interface is formed within the region spanning amino acids 1-90 where K-Ras4B^{G12V} and H-Ras^{E31K} share 100% amino acid sequence identity except for the point mutations G12V and E31K.

The K-Ras4B^{G12V}:Rgl2^{RBD} heterotetramer complex is stabilized by a network of hydrogen bonds and hydrophobic interactions (Fig. 2B, C and D, Supplementary Fig. S3A), leading to a complimentary surface charges (Supplementary Fig. S3B). K-Ras4B^{G12V} residues within the Switch I interact with residues in β1, β2 and α1 of Rgl2^{RBD}. These interactions include a salt bridge between E37 of K-Ras4B^{G12V} Switch I and R653 of Rgl2^{RBD} (Fig. 2B and Supplementary Fig. S3A). The Switch II of the same K-Ras4B^{G12V} molecule also contributes to complex formation by interacting with the second Rgl2^{RBD} through residues in β2 and α1 (Fig. 2B and Supplementary Fig. S3A). Meanwhile, two K-Ras4B^{G12V} molecules have direct contact through the Switch I, Switch II and α3 (Fig. 2C and Supplementary Fig. S3A). Strikingly, the V12 residue of the oncogenic G12V mutation is within 4 Å of the ring of Y32 of the neighboring K-Ras4B^{G12V} contributing to the K-Ras4B^{G12V}: K-Ras4B^{G12V} interface (Fig. 2C and Supplementary Fig. S3). The β1 of both Rgl2^{RBD} molecules run anti-parallel to each other, interacting through various hydrophobic interactions and hydrogen bonds at both side-chain and backbone levels (Fig. 2D).

Solution NMR analyses support the K-Ras4B^{G12V}:Rgl2^{RBD} heterotetramer formation

The K-Ras4B^{G12V}:Rgl2^{RBD} complex was further analyzed in solution. First, the solution structure of the Rgl2^{RBD} construct was determined by solution NMR (Fig. 3A) (Table 2). The structure retained the ββαββαβ ubiquitin-fold structure, a common feature for the RBDs (34). Overall, it is similar to Rlf, the mouse homologue of human Rgl2 (PDB ID 1RLF)(35). However some differences can be observed, even though the primary sequences are similar (Supplementary Fig. S4A). The structures of the Rgl2^{RBD} molecules in the K-Ras4B^{G12V}:Rgl2^{RBD} complex crystal structure are highly comparable with the structure of the NMR solution structure of free Rgl2^{RBD} indicating that the complex formation causes relatively small structural changes (Fig. 3B).

The K-Ras4B^{G12V}:Rgl2^{RBD} complex was next analyzed in solution by NMR chemical shift perturbation. Two-dimensional (2D) ^{15}N–^{1}H-heteronuclear single quantum coherence (HSQC) spectrum were measured of ^{15}N-labelled Rgl2^{RBD} sample, in the absence or presence of increasing amount of non-labelled K-Ras4B^{G12V} (Fig. 3C, Supplementary Fig.S4B and C). Chemical shift perturbations were observed for most of the Rgl2^{RBD} residues, in agreement with K-Ras4B^{G12V}:Rgl2^{RBD} complex formation in solution (Supplementary Fig.S4B and C). Most of the Rgl2^{RBD} residues at the K-Ras4B^{G12V}:Rgl2^{RBD} and Rgl2^{RBD}:Rgl2^{RBD} interfaces in the crystal structure showed a greater change (either decreased or increased) in their NMR signal intensities, indicating their participation to the complex formation (Fig. 3C). Notably, signals from the Rgl2^{RBD} residues in β1 at the N-terminal end made the largest increase. An explanation may be that the highly flexible N-terminal region of free Rgl2 (Fig. 3A) becomes confined into a more defined structure upon complex formation as observed in the crystal structure.

It has been shown that a lysine residue of RALGDS, that corresponds to K686 of Rgl2, plays an essential role in H-Ras^{E31K}:RALGDS complex formation (29)(Supplementary Fig. S5A). In the K-Ras4B^{G12V}:Rgl2^{RBD} complex crystal structure, K686 forms a hydrogen bond with D33 of K-Ras4B^{G12V} (Supplementary Fig. S5B). K686 was also among the residues that showed a substantial signal decrease in the NMR titration assays (Fig. 3C). We therefore mutated K686 into an alanine and as expected the K686A mutant lost the ability to interact with K-Ras4B^{G12V} (Supplementary Fig. S5C), confirming the important role of K686 in the interaction.

We next examined the NMR chemical shift perturbation of K-Ras4B^{G12V} in solution by 2D ^{15}N–^{1}H-HSQC, in absence or presence of non-labelled Rgl2^{RBD}. We noticed that when loaded with GMPPNP, the number of detectable peaks of the ^{15}N labelled K-Ras4B^{G12V} signal was

substantially decreased compared to the number of signals obtained from the GDP-loaded sample (Supplementary Fig. S6) as previous studies reported (36, 37). Consequently, most of the K-Ras4B^{G12V} residues at the K-Ras4B^{G12V}:Rgl2^{RBD} complex interface could not be detected, except for K42 and K88, both of which were showing substantially decreased signal intensities, in agreement with the expected participation in the complex formation (Supplementary Fig. S7). Furthermore, upon Rgl2^{RBD} titration, most of the ^{15}N K-Ras4B^{G12V} signals were reduced (Supplementary Fig. S7). This overall signal reduction was consistent with broadening arising as a result of the large complex size.

Mass photometry confirms the presence of a heterotetramer of K-Ras4B^{G12V}:Rgl2^{RBD} complex

To confirm that K-Ras4B^{G12V}:Rgl2^{RBD} forms a heterotetramer in solution, we analyzed the complex by mass photometry, a label free technique that has recently been adapted to measure the mass of biomolecules in solution (38). Our commercially-available instrument (see Materials and methods) can measure accurately masses in the range 30-5000 kDa, and is suitable to differentiate between K-Ras4B^{G12V}:Rgl2^{RBD} heterodimer (31kDa) or heterotetramer (62kDa). The K-Ras4B^{G12V}:Rgl2^{RBD} complex was freshly prepared by size exclusion chromatography and the peak fraction that contained both proteins at 1:1 ratio was used for the measurement (Fig. 4A). The histogram of the frequency counts for this sample showed a peak, that after calibration with the proper standard (Native Mark) , corresponds to a biomolecule with molecular weight of 68 KDa (Fig. 4B). As the expected molecular weight of the K-Ras4B^{G12V}:Rgl2^{RBD} heterotetramer is about 62 KDa, the result strongly indicates that at least part of the complex population exists as the 2:2 heterotetramer in solution.

Discussion

We conducted interaction studies of human K-Ras4B and Rgl2^{RBD} to obtain structural insights into the oncogenic Ras-dependent activation of the RalA/B pathway. Using X-ray crystallography and the crystal structure of human H-Ras^{E31K} and rat RALGDS complex (PDB ID 1LFD) as a molecular replacement template (29), we reveal a heterotetramer formation stabilised by the oncogenic G12V mutation. The presence of heterotetramer in solution was further confirmed by mass photometry.

Mode of interaction between Ras and Rgl2/RALGDS is distinct from other Ras:RBD interactions

The key contributor of the heterotetramer formation seen in this Ras:RalGEF complex, K-Ras4B^{G12V}:Rgl2^{RBD}, and the previously published H-Ras^{E31K}:RALGDS^{RBD} is the interaction between the Switch II region of Ras and the second RBD molecule (Fig. 2B and Supplementary Fig. S8 A). This feature is distinct from the previously reported Ras:RBD crystal structures, where the Switch II region is either not participating in the interaction (as seen in Ras:Raf1^{RBD} (PDB ID 6VJJ)(39)) or is interacting with an RBD that also interacts with the Switch I region of the same Ras molecule (as seen in Ras:PI3Kγ^{RBD} (PDB ID 1HE8)(40), Ras: PLCε^{RBD} (PDB ID 2C5L)(41), Ras:RASSf5^{RBD} (PDB ID 3DDC)(42)), hence forming a Ras:RBD heterodimer, rather than a heterotetramer, in each crystal lattice (Supplementary Fig. S8B). One interesting case is a recently reported structural study of Rgl1, yet another RalGEF (43). Crystal structures of Rgl1 in complex with either K-Ras^{WT} or K-Ras^{G12V} (PDB ID 7SCW and 7SCX, respectively), showed that one Rgl1^{RBD} interacts with one K-Ras molecule through both Switch I and Switch II, as other heterodimer examples shown in Fig. S8B. It will be interesting to further examine whether the K-Ras:Rgl1^{RBD} may have the capacity to form a heterotetramer as a common feature for Ras:RalGEF complexes.

Oligomerisation of K-Ras:effector complexes

Accumulating evidence suggests that K-Ras is capable of forming a dimer in solution even in the absence of effectors (44-53). The physiological importance of Ras dimerisation and its potential to be a therapeutic target was highlighted by a G12D-specific inhibitor, BI2852, which may cause artificial dimerisation and block the protein function (54, 55). Furthermore, Ras forms nanoclusters in the membrane *in vivo* and *in vitro* (56-60). The modes of these Ras oligomer formation are dependent on various parameters including membrane lipid compositions, Ras nucleotide binding status, availability of Ras effectors and actin cytoskeleton and are expected to be context dependent.

Previously it has been suggested that dimerisation status may be categorised into four classes based on the utilized α helices and β sheets as follows; (i) α4/α5 (44, 45, 47, 48, 50, 52), (ii) α3/α4 (48, 50, 51), (iii) α/β (47), and (iv) β/β (48, 51) (Supplementary Fig. S9). Importantly, the K-Ras4B^{G12V}:K-Ras4B^{G12V} interface that we observe in the K-Ras4B^{G12V}:Rgl2^{RBD} heterotetramer

does not belong to any of these categories and uses unstructured regions of Switch I, Switch II, V12 in the P-loop and K88 (Fig. 2, Supplementary Fig. S2 and Fig. S9). Interestingly, this K-Ras4B^{G12V}:K-Ras4B^{G12V} interface is similar to the spatial arrangement of symmetry mates of human H-Ras^{WT} crystal (PDB ID 5P21) (61) (Supplementary Fig. S10), indicating that this Ras:Ras contact is likely stabilized by Rgl2^{RBD}.

Currently, we do not have information as to the orientation of the K-Ras4B^{G12V}:Rgl2^{RBD} in relation to the plasma membrane (PM). The Rgl2 molecules could be away from the plasma membrane (PM-away conformation), or could be in direct contact with the plasma membrane (PM-proximity conformation) (Supplementary Fig. S11). In either case, the complex status is distinct from the case for Ras:Raf1 kinase complex which can be formed onto the existing Ras:Ras homodimer of the $\alpha4/\alpha5$ interface (45). If the majority of the cellular K-Ras4B^{G12V} molecules exist as the $\alpha4/\alpha5$ homo-dimer at the PM, what drives the K-Ras4B^{G12V}:Rgl2^{RBD} heterotetramer formation by causing a major structural change is an important future question.

Direct involvement of V12 in the K-Ras4B:Rgl2^{RBD} complex formation and oncogenicity

Strikingly, the K-Ras4B^{G12V}:K-Ras4B^{G12V} interface of the K-Ras4B^{G12V}:Rgl2^{RBD} tetramer complex involves the residue V12, an oncogenic amino-acid substitution occurring in about 28% of mutated *KRAS* cases (COSMIC). This G12V substitution substantially increases the affinity towards Rgl2^{RBD} compared to the wildtype (Fig. 1B). In agreement with this observation, our attempt to biochemically purify the K-Ras4B^{WT}:Rgl2^{RBD} complex has been unsuccessful as K-Ras4B^{WT} and Rgl2^{RBD} eluted in separate fractions when subjected to size exclusion chromatography (data not shown). In the K-Ras4B^{G12V}:Rgl2^{RBD} tetramer complex, the presence of V12 creates a larger hydrophobic pocket together with Y32, compared to the wildtype case of G12, seen in the H-Ras^{WT} crystal (PDB ID 5P21) or in the H-Ras^{E31K}:RALGDS^{RBD} crystal (PDB ID 1LFD) (Supplementary Fig. S10 and S12). To our knowledge, the K-Ras4B^{G12V}:Rgl2^{RBD} complex serves as the first example where a structural explanation is provided for an oncogenic-Ras driven stabilization of a Ras:effector complex. Interestingly, the E31K substitution, used in the H-Ras^{E31K}:RALGDS crystal structure analysis to stabilize the complex (29) (Supplementary Fig. S12E), has been reported in cancer samples with *HRAS* mutation (COSMIC). Therefore, the capability of Ras to form a stable complex with RalGEFs may be directly linked with Ras oncogenicity. It is interesting to note that in the previously proposed Ras:Raf1 kinase

heterotetramer complex derived from SAXS data (45), the position of the amino acid residue 12 is relatively distant from the interacting surfaces. An interesting speculation could be that the oncogenic substitution mutations at glycine 12 might have a greater impact on RalGEF-mediated signalling than Raf kinase-mediated signalling (Supplementary Fig. S11).

Conclusion

To summarize, our work demonstrates an increased affinity of K-Ras4B^{G12V} oncogenic mutant with a RalGEF, Rgl2, and provides a structural explanation by revealing the complex interface. The information will open the way to target oncogenic-*KRAS*-induced tumorigenesis by novel strategies, including interfering molecules for the newly identified interfaces.

Materials and Methods

Plasmid constructs

The RBD of human Rgl2 was obtained by amplifying a cDNA fragment encoding the position 643 – 740 of the human Rgl2 by PCR with a pair of primers (5' TACTTCCAATCCATGGGGCCAGGGGCCTCTGATTGCCG3') and (5' TATCCACCTTTACTGTCA TGTAGCAGTAGAGGACCTTCGCCGCTGC 3') using human cDNA prepared from hTERT RPE-1 cells using GoScript Reverse Transcription System (Promega) following the manufacturer's instruction. The amplified $Rgl2^{RBD}$ fragment was cloned into pLEICS2 vector (PROTEX, University of Leicester), which contains a glutathione S-transferase (GST) affinity tag and a Tobacco Etch virus (TEV) potease cleavage site at the N-terminal end of the $Rgl2^{RBD}$, using In-Fusion HD EcoDry enzyme (Takara Bio, #638915), following the manufacturer's instruction. A point mutation, K686A, was introduced by site-directed mutagenesis using a pair of primers (5' ATCAGTCGTGTCCTTAAGGCAAACAATCGTGACTCT 3') and (5' CAGAGTCACGATTGTTTGCCTTAAGGACACGACTGAT 3') by following the QuikChange™ method (Agilent Technologies, La Jolla, CA, USA).

A cDNA fragment encoding the position 1 – 169 (C-terminal truncated) of the human wildtype K-Ras4B isoform was amplified by PCR with a pair of primers (5' TACTTCCAATCCATG ACTGAATATAAACTTGTGGTAGTTGGAGCTG') and (5' TATCCACCTTTACTGTCA CTTTTCTTTATGTTTTCGAATTTCTCGAACTAATGTATAG 3') using human cDNA prepared from hTERT RPE-1 cells as described above. The produced fragment was cloned in pLeics1 plasmid (PROTEX, University of Leicester), which introduces a His6 tag and a TEV cleavage site at the N-terminus. Site directed mutagenesis was conducted to introduce the oncogenic G12V mutation using a pair of DNA oligos (5' AGTTGGAGCTGTTGGCGTAGGCAAGAGTGCC 3') and (5' GTCAAGGCACTCTTGCCTACGCCAACAGCTCCAACTAC 3') by following the QuikChange™ method (Agilent Technologies, La Jolla, CA, USA).

Protein expression

DE3 Rosetta cells (Novagen) carrying expression plasmids were grown at 37°C in TY media until OD600 reached about 0.6. Then protein expression was induced by adding Isopropyl β-D-1-thiogalactopyranoside (IPTG) to a final concentration of 0.5 mM and keeping the culture at 18°C overnight in a shaking incubator. Cells were collected by centrifugation and resuspended in

either Sl1 buffer (Tris 20mM (pH 7.65), NaCl 150 mM, 5 mM imidazole) for His-tagged KRas or in PBS-NaCl buffer (237 mM NaCl, 2.7 mM KCl, 8 mM Na_2HPO_4, and 2 mM KH_2PO_4, pH 7.4) for Rgl2 and RalGDS. The cell suspensions were then stored at -80°C.

Protein expression of stable isotope labelling K-Ras4B^{G12V} and RBD of Rgl2 for NMR measurement

The gene encoding human K-Ras4B^{G12V} and Rgl2^{RBD} were constructed into the expression vector pGHL9 and pLEICS2 over-expressed in *Escherichia coli* (*E.coli*) strain BL21 (DE3) and Rosetta, respectively. Uniformly ^{13}C, ^{15}N-labeled protein was obtained by growing bacteria at 37 °C in M9 minimal media, containing [$^{13}C_6$]-glucose and $^{15}NH_4Cl$ (Isotec) as the sole carbon and nitrogen source, supplemented with 20 mM $MgSO_4$, 0.1 mM $CaCl_2$, 0.4 mg/ml thiamin, 20 μM $FeCl_3$, salt mix [4 μM $ZnSO_4$, 0.7 μM $CuSO_4$, 1 μM $MnSO_4$, 4.7 μM H_3BO_3], and 50 mg/L ampicilin. K-Ras4B^{G12V} NMR sample was prepared essentially as described previously (37). Protein expression of Rgl2^{RBD} was induced by adding 119mg/L IPTG at an OD 600 nm of 0.5. After 18 h of further growth, cells were harvested, and washed with a pH 7.5 lysis buffer [50 mM Tris-HCl, 25% sucrose, and 0.01% NP-40]. Uniformly ^{15}N-labeled K-Ras4B^{G12V} and Rgl2^{RBD} were produced by the identical steps unless growing cells in M9 medium containing [$^{12}C_6$]-glucose and $^{15}NH_4Cl$ (Isotec).

Purification of GST-tagged Rgl2^{RBD}

Bacteria cell suspensions were thawed and supplemented with Triton X-100 to a final concentration of 0.1 % (v/v). Cells were broken by a probe sonicator and insoluble materials were removed by centrifugation. The supernatant was mixed with glutathione (GSH) beads (GE Healthcare, #17-0756-01) and incubated for 20 min at 4°C. The GSH beads were washed three times with the PBS-NaCl buffer. the GST-Rgl2^{RBD} fusion protein was either eluted by the elution buffer (50mM Tris-Cl (pH 8.0), 100mM NaCl, 5mM GSH) for GST pulldown experiments or the Rgl2^{RBD} was separated from the GST tag through cleavage by tobacco etch virus (TEV) protease, which was prepared as previously described (62, 63), for structural analysis. The obtained Rgl2^{RBD} or GST-Rgl2^{RBD} fusion proteins were concentrated using a concentrator (10 kDa MWCO, Merck, Amicon Ultra centrifugal filters, #UFC901024) and filtrated using a centrifugal filter unit (Milipore, Ultrafree, #UFC30GV00) before conducting size exclusion chromatography (SEC) with a gel-filtration column (GE Healthcare, HiLoad Superdex 75) attached to an FPLC (Akta) system.

SEC was carried out in a gel filtration buffer (20 mM Tris-Cl (pH 7.65), 100 mM NaCl, 5mM MgCl2, 1mM tris (2-carboxyethyl) phosphine (TCEP)).

Purification of His-tagged K-Ras4B wildtype and oncogenic G12V mutant proteins

Bacteria cell suspensions were supplemented with Triton X-100 to a final concentration of 0.1 % (v/v). Cells were broken by a probe sonicator and insoluble materials were removed by centrifugation. The soluble cell lysates were applied on a Ni-sepharose excel (GE Healthcare, #17-3712-01), packed in a column of 4 ml bed volume with Sl1 buffer buffer (20mM Tris, pH6.5, 150mM NaCl, 5 mM imidazole). The column was washed with 20 ml of SL1 Buffer, then with 20 ml of Sl3 Buffer (20mM Tris, pH6.5, 150mM NaCl, 6mM Imidazole) and finally with 15 ml of Sl4 Buffer (20mM Tris, pH6.5, 150mM NaCl, 10mM Imidazole). The His-tagged Kras protein was eluted from the column by applying 10 ml of Elution buffer (50mM Tris, pH 7.65, 150mM NaCl, 200mM Imidazole), followed by 10 ml of 1 M imidazole. In order to remove the His6-tag at the N-terminal end, TEV protease, prepared as previously described (63), was added to the elution fraction to about a 2 % molar ratio of the His6-K-Ras4B preparation and incubated overnight at 4°C. Nucleotide exchange of the purified K-Ras4B wildtype or G12V proteins was carried out essentially as previously described (37). The proteins were diluted 10 times by the exchange buffer (20mM Tris-Cl (pH7.5) 1mM EDTA, 1mM TECP) and denatured by the addition of EDTA to a final concentration of 5 mM. The sample was mixed with about 10 time molar excess of guanosine 5'-[β,γ-imido]triphosphate (GMMPPNP, SIGMA G0635) or guanosine 5' –diphosphate (GDP, SIGMA G7127). The reaction was incubated at 37℃ for 20 minutes then put it on ice for 20 minutes. The protein was renatured by adding ice cold $MgCl_2$ to a final concentration of 20 mM.

Purification of isotope labelling K-Ras4B^{G12V}

All the procedures described below were carried out at 4 °C unless otherwise stated. All the isotope-labelled K-Ras4B^{G12V} samples were purified by the same step. The cells dispersed in the lysis buffer was disrupted by sonication for 30 min on ice with hen egg lysozyme (0.1 mg/mL). The cell debris was clarified by centrifugation at 14,000 g for 1 h. The supernatant was loaded onto a 25 mL of DEAE-Sepharose Fast Flow (Cytiva) anion exchange equilibrated with buffer A [50 mM Tris-HCl (pH 7.5), 1 mM $MgCl_2$, 1 mM dithiothreitol (DTT), 0.1 mM APMSF (FUJIFILM Wako)]. After washing the column with buffer A until sufficiently low of UV absorption at 280

nm, the K-Ras4B^{G12V} protein was eluted by linearly increasing the concentration of KCl from 0 to 350 mM with a flow rate of 0.5 mL/min in buffer A. The fractions containing the target protein were concentrated to 5 mL with Amicon Ultra-15 10 kDa (Merck). The concentrated sample was loaded onto a 320 mL of HiLoad Superdex 75 (GE Healthcare Life Science) gel filtration with a flow rate of 0.8 mL/min using FPLC systems (AKTA pure 25, GE Healthcare Life Science). The 5 mL sample concentrated from the fractions involving the target proteins with Amicon Ultra-15 10 kDa was loaded on Resource Q (GE Healthcare Life Science) anion-exchange column equilibrated with buffer A using the FPLC systems. After washing the column with 30 mL of buffer A, K-Ras4B^{G12V} was eluted by an KCl, the K-Ras4B^{G12V} protein was eluted by linearly increasing the concentration of KCl from 0 mM to 350 mM with a flow rate of 1 mL/min in buffer A. The purification of isotope labelled Rgl2^{RBD} was pefromed by the same step described above. The purity of the K-Ras4B^{G12V} and Rgl2^{RBD} samples in each step was confirmed by SDS-PAGE. Protein concentrations were determined by NanoDrop 2000 (ThermoFisher) measuring UV absorption at 280 nm. K-Ras4B^{G12V} samples for NMR measurements were concentrated and dissolved in NMR buffer A (90% $^{1}H_2O$/ 10% $^{2}H_2O$ containing 20 mM Tris-HCl (pH 7.5), 100 mM NaCl, 5 mM $MgCl_2$, 1 mM β-mercaptoethanol). Rgl2^{RBD} samples for NMR measruments were NMR buffer B (90% $^{1}H_2O$/ 10% $^{2}H_2O$ containing 1 mM Na_2HPO_4-NaH_2PO_4 (pH 7.4), 150 mM NaCl).

K-Ras4B-Rgl2^{RBD} binding measurement using BLI

Octet Red96 (Sartorius) was used for Biolayer interferometry assays of KRas4B (G12V or WT) and Rgl2^{RBD} interactions. Anti-GST biosensors (Sartorius #18-5096) were used to immobilise GST-Rgl2^{RBD}, and baseline was stabilised in BLI buffer (20mM Tris pH7.65, 0.5mM NaCl, 5mM MgCl, 1mM TCEP) for 200sec. The association of KRas4B was measured for 300sec in 6 serial dilutions concentrations. For KRas (WT) the concentrations used ranged from 625 nm - 10 µM and for KRas4B (G12V) the concentrations ranged from 200 nM – 6.4 µM. The dissociation steps were measured in fresh BLI buffer for 300sec. For each assay a biosensor immobilised with GST only and a sample well with only buffer instead of KRas4B (WT/G12V) was set up. The experiments were conducted at 23°C. The resulting data were processed using Data Analysis HT Software (ver. 12.0.2.59)(FORTE BIO) and reference biosensor and reference wells were subtracted from sample wells. A 1:1 global fitting model was used with sensor type to fit steady state curves to determine K_D values.

Analysis of bound nucleotide

The nucleotide-binding status of K-Ras4B^{WT} and K-Ras4B^{G12V} were examined by denaturating the proteins and detecting the released nucleotides (64). About 2 nmoles of K-Ras4B molecules were adjusted to the volume of 200 µl with AKTA buffer. Add 12.5 µl of 10% perchloric acid to denature the protein. Add 8.75 µl of 4M CH_3COONa, pH 4.0, to neutralise the sample and centrifuge it to precipitate the denatured protein. The supernatant was analysed by High-performance liquid chromatography (HPLC) using an ion-exchange column (Partisil 10 SAX column, Whatman) equilibrated with 10 mM NH_4H2PO_4 (buffer A). The column was run with the following gradient condition with 0.6 M NH_4H2PO_4 (buffer B) at a flow rate of 0.8 ml/min. Step1: 100% buffer A (0% buffer B) for 11 min, Step2: a gradient increase to 40% buffer B over 6 min, Step3: a gradient increase to 50% buffer B over 23 min, Step4: a gradient increase to 100 % buffer B over 1 min, Step 5: 100 % buffer B for 19 min, Step 6: a gradient decrease to 0% buffer B (100 % buffer A) over 1 min, and Step 7: 100% Buffer A for 14 min. The nucleotides were detected by 254 nm absorption. As a reference control, 1 µl of 10 mM GTP or GDP was diluted to 200 µl AKTA buffer and was processed in the same manner as protein samples.

Crystallography

The purified and GMPPNP-loaded KRas4B (G12V) and Rgl2^{RBD} were mixed in gel filtration buffer and the complex was purified on SEC using a gel-filtration column (GE Healthcare, HiLoad Superdex 75). The peak fractions containing both proteins in the 1:1 ratio were collected and concentrated to set up crystallization screenings. Crystals of KRas4B (G12V) and Rgl2^{RBD} were obtained using sitting-drop vapour diffusion at room temperature, with 100nl of protein (11.6mg/ml) against 100nl of crystallisation buffer (0.2M sodium/potassium phosphate ph 7.5, 0.1M HEPES pH 7.5, 22.5% v/v PEG smear Medium (Molecular Dimensions MD2-100-259), 10% v/v glycerol. The crystals were frozen in liquid nitrogen with 20% glycerol as cryoprotectant. Data were collected at Diamond beamline I04. AIMLESS (65) was used for data reduction before obtaining phaser solution using the HRas-RALGDS^{RBD} complex structure (PDB ID 1LFD) as search model with PhaserMR (66). The structure was built using multiple rounds of refinements using PDBredo, REFMAC, PHENIX and COOT (32, 33, 67, 68). The coordinates of the complex have been deposited to the Protein Data Bank (PDB) under access code 8B69.

Circular dichroism (CD) spectroscopy

K-Ras4B(WT) and (G12V) proteins at a concentration of 20 µM were prepared in the CD buffer (50 mM phosphate (pH 7.6), 1.5 mM tris (pH 7.6), 5mM MgSO4, 7.5 mM NaCl, 0.375 mM MgCl2), placed in a quartz cuvette of 0.1 cm path length and CD spectra were recorded at wavelengths ranging from 195 to 250 nm using a Chirascan^{TM}-plus CD spectrometer (Applied Photophysics) at 20 °C. The melting curves of these proteins were examined at 220 nm at temperatures ranging from 20°C to 90°C. Measurements were conducted at 1 ^{o}C increment.

NMR spectroscopy

K-Ras4B^{G12V} NMR sample was prepared essentially as described previously (37). The bacteria expression plasmid for H-Ras was modified to encode K-Ras4B^{G12V} by site-directed mutagenesis and used to produce K-Ras4B^{G12V}. Loading of a GTP analogue, GMPPNP (Jena Bioscience) was conducted essentially as previously described (37). Rgl2^{RBD} sample was prepared as described above. All NMR samples were measured in 20 mM Tris-Cl (pH 7.65), 100 mM NaCl, 5mM $MgCl_2$, and 0.1% β-mercaptoethanol at 303 K. All spectra were analysed with the CcpNmr Analysis 2.5.1 software. Backbone chemical shifts of K-Ras4B^{G12V} and Rgl2 have been deposited to the BioMagResBank with accession ID 34754 and Protein Data Bank with accession ID 8AU4, respectively.

All NMR experiments were performed at 25°C probe temperature in a triple-resonance cryoprobe fitted with a z-axis pulsed field gradient coil, using Bruker AVANCE-III HD 600 MHz spectrometers. All spectra were processed with the Azara software package (69). For the 3D data, the two-dimensional maximum entropy method (2D MEM) or Quantitative Maximum Entropy (QME) (70) were applied to obtain resolution enhancement for the indirect dimensions. All NMR spectra were visualized and analyzed using the CcpNmr Analysis 2.5.0 software (71). All of the 3D triple-resonance experiments used for the assignments of K-Ras4B and Rgl2^{RBD} were performed on $^{13}C/^{15}N$ samples in NMR buffer A and B, respectively. The backbone $^{1}H^{N}$, $^{13}C'$, and ^{15}N for K-Ras4B and Rgl2^{RBD}, and side-chain $^{13}C^{\alpha}$ and $^{13}C^{\beta}$ resonance assignments for Rgl2^{RBD} were achieved by analyzing six types of 3D triple-resonance experiments, HNCO, HN(CA)CO, HNCA, HN(CO)CA, CBCANNH, and CBCA(CO)NNH. 3D HBHA(CBCACO)NH, H(CCCO)NH, (H)CC(CO)NH, HCCH-COSY, and HCCH-TOCSY experiments on the $^{13}C/^{15}N$ -labeled Rgl2^{RBD} were performed for side-chain ^{1}H and ^{13}C resonance assignments. A 15 ms ^{13}C isotropic mixing time was employed

for the (H)CC(CO)NH, H(CCCO)NH and HCCH-TOCSY experiments. For the collection of NOE-derived distance restraints of Rgl2^{RBD}, 3D ^{15}N-separated and 3D ^{13}C-separated NOESY-HSQC spectra were measured on the ^{13}C/^{15}N -labeled Rgl2^{RBD}. A 100 ms NOE mixing period was employed for the 3D NOESY experiments. All 2D and 3D NMR data were recorded using the States-TPPI protocol for quadrature detection in indirectly observed dimensions. Water flip-back ^{1}H pulses and the WATERGATE pulse sequence were used for solvent suppression in the experiments performed on ^{15}N-labeled, and ^{13}C/^{15}N-labeled samples, whereas presaturation and gradient-spoil pulses were used for ^{13}C-labeled samples.

A series of 2D ^{1}H-^{15}N HSQC spectra were measured for titration experiments of ^{15}N-labelled K-Ras4B^{G12V} with in the presence of non-labelled Rgl2^{RBD}. The experiments were performed in the NMR buffer at 25 °C and the peptide concentration was increased stepwise (for the ^{15}N-K-Ras4B^{G12V} / Rgl2^{RBD}, its molar ratio of 1:0.25, 1:0.5, 1:0.75, 1:1, 1:1.5, and 1:2 were used, while for the ^{15}N-Rgl2^{RBD} / K-Ras4B^{G12V}, its molar ratio of 1:0.25, 1:0.5, 1:1, 1:1.5, 1:2, and 1:3 were used). The mean chemical shift difference $\Delta\delta_{ave}$ for each amino acid was calculated as $[(\Delta\delta^{1}H^{N})^{2} + (\Delta\delta^{15}N)^{2}]^{1/2}$ where $\Delta\delta^{1}H^{N}$ and $\Delta\delta^{15}N$ are the chemical shift differences (Hz) between K-Ras4B^{G12V} or Rgl2^{RBD} on their own and the proteins in the presence of the other side.

NMR structure calculation

Intra-residual and long-range NOEs were automatically assigned by the program CYANA with the use of automated NOE assignment and torsion angle dynamics (72). The peak position tolerance was set to 0.03 ppm for the 1H dimension and to 0.3 ppm for the 13C and 15N dimensions. Hydrogen-bond and dihedral angle restraints were not used. CYANA calculations were started from 100 conformers with random torsion angle values, simulated annealing with 50,000 torsion angle dynamics steps was applied. The 20 conformers with the lowest final target-function values of CYANA were selected and optimised with OPALp 2.1 [22,23] using the AMBER force field [24,25]

Mass photometry measurement

Freshly purified KRas4B (G12V) and Rgl2^{RBD} were mixed in AKTA buffer, concentrated to about 500 µl using a concentrator (Merck, Amicon Ultra centrifugal filters, #UFC901024), and loaded to

a gel-filtration column (GE Healthcare, HiLoad Superdex 75). The peak fractions containing both proteins in the 1:1 ratio were collected and the concentration was estimated by OD_{280} and the predicted extinction coefficient of 24155 $M^{-1}cm^{-1}$. The sample was diluted to 40 nM in gel filtration buffer and a 20 µL aliquot was subjected to mass photometry (OneMP, Refeyn). The measurement was done in conventional microscope cover glass (Marienfeld, nº 1.5H) cleaned by rinsing with deionized water (×5) and isopropanol (×5) followed by drying under a N_2 flow, using a silicon gasket (Grace Bio-labs) in order to confine the sample. Adsorption of individual molecules of complex was detected across an imaging area of 10.8 µm by 2.9 µm.

Video recordings from interferometric scattering microscopy for a duration of 60s were obtained and the single events corresponding to surface adsorption of the complex were identified using AcquireMP software (Refeyn). Data analysis was performed using DiscoverMP software (Refeyn) and OriginPro 2021 (OriginLab).

Graphical representation of protein structures

Protein structure images were generated using Pymol (The PyMOL Molecular Graphics System, Version 1.2r3pre, Schrödinger, LLC). Electrostatic surface charge potential images were produced using Pymol vacuum electrostatics function. Amino acid residues in the interaction surfaces of protein complexes in a PDB format were predicted using LIGPLOT (73).

Acknowledgments

We thank the help and expert advice from the University of Leicester colleagues Peter Moody, Thomas Schalch, Ian Eperon, Mohammed Bhogadia, Luke Bailey, Kyle Daynes, Idir Malki, and Ziad Ibrahim. Biolayer interferometry experiments were conducted with the guidance of Holly Birchenough and Thomas Jowitt (Biomolecular Analysis Core Facility, University of Manchester).

We gratefully acknowledge financial support from Wellcome Trust ISSF COVID career support and inclusion scheme 204801/Z/16/Z and University of Leicester MSc program M32DF74 (to K.T.), University of Leicester College PhD programme M32RT742 (to M.T.), the Funding Programs for Core Research for Evolutional Science and Technology (CREST; JPMJCR13M3 to Y.I., JPMJCR21E5 to T.I.) the Japan Science and Technology Agency (JST), Grants-in-Aid for Scientific Research (JP15K06979 to T.I., JP19H05645 to Y.I.) and Scientific Research on Innovative Areas

(JJP15H01645, JP16H00847, JP17H05887 and JP19H05773 to Y.I. P26102538, JP25120003, JP16H00779 and JP21K06114 to T.I.) from the Japan Society for the Promotion of Science (JSPS), Shimazu foundation, and the Precise Measurement Technology Promotion Foundation.

References

1. Cox AD & Der CJ (2010) Ras history: The saga continues. *Small GTPases* 1(1):2-27.
2. Vetter IR & Wittinghofer A (2001) The guanine nucleotide-binding switch in three dimensions. *Science* 294(5545):1299-1304.
3. Simanshu DK, Nissley DV, & McCormick F (2017) RAS Proteins and Their Regulators in Human Disease. *Cell* 170(1):17-33.
4. Castellano E & Santos E (2011) Functional specificity of ras isoforms: so similar but so different. *Genes Cancer* 2(3):216-231.
5. Newlaczyl AU, Coulson JM, & Prior IA (2017) Quantification of spatiotemporal patterns of Ras isoform expression during development. *Sci Rep* 7:41297.
6. Gibbs JB, Sigal IS, Poe M, & Scolnick EM (1984) Intrinsic GTPase activity distinguishes normal and oncogenic ras p21 molecules. *Proc Natl Acad Sci U S A* 81(18):5704-5708.
7. McGrath JP, Capon DJ, Goeddel DV, & Levinson AD (1984) Comparative biochemical properties of normal and activated human ras p21 protein. *Nature* 310(5979):644-649.
8. Der CJ, Finkel T, & Cooper GM (1986) Biological and biochemical properties of human rasH genes mutated at codon 61. *Cell* 44(1):167-176.
9. Bollag G & McCormick F (1991) Differential regulation of rasGAP and neurofibromatosis gene product activities. *Nature* 351(6327):576-579.
10. Scheffzek K*, et al.* (1997) The Ras-RasGAP complex: structural basis for GTPase activation and its loss in oncogenic Ras mutants. *Science* 277(5324):333-338.
11. Manne V, Bekesi E, & Kung HF (1985) Ha-ras proteins exhibit GTPase activity: point mutations that activate Ha-ras gene products result in decreased GTPase activity. *Proc Natl Acad Sci U S A* 82(2):376-380.
12. Smith MJ & Ikura M (2014) Integrated RAS signaling defined by parallel NMR detection of effectors and regulators. *Nat Chem Biol* 10(3):223-230.
13. Mazhab-Jafari MT*, et al.* (2015) Oncogenic and RASopathy-associated K-RAS mutations relieve membrane-dependent occlusion of the effector-binding site. *Proc Natl Acad Sci U S A* 112(21):6625-6630.
14. Hunter JC*, et al.* (2015) Biochemical and Structural Analysis of Common Cancer-Associated KRAS Mutations. *Mol Cancer Res* 13(9):1325-1335.
15. Pantsar T*, et al.* (2018) Assessment of mutation probabilities of KRAS G12 missense mutants and their long-timescale dynamics by atomistic molecular simulations and Markov state modeling. *PLoS Comput Biol* 14(9):e1006458.
16. Maurer G, Tarkowski B, & Baccarini M (2011) Raf kinases in cancer-roles and therapeutic opportunities. *Oncogene* 30(32):3477-3488.
17. Chalhoub N & Baker SJ (2009) PTEN and the PI3-Kinase Pathway in Cancer. *Annual Review of Pathology: Mechanisms of Disease* 4(1):127-150.
18. Tuveson DA*, et al.* (2004) Endogenous oncogenic K-ras(G12D) stimulates proliferation and widespread neoplastic and developmental defects. *Cancer Cell* 5(4):375-387.
19. Yip-Schneider MT, Lin A, & Marshall MS (2001) Pancreatic tumor cells with mutant K-ras suppress ERK activity by MEK-dependent induction of MAP kinase phosphatase-2. *Biochem Biophys Res Commun* 280(4):992-997.

20. Yip-Schneider MT, Lin A, Barnard D, Sweeney CJ, & Marshall MS (1999) Lack of elevated MAP kinase (Erk) activity in pancreatic carcinomas despite oncogenic K-ras expression. *Int J Oncol* 15(2):271-279.
21. Luo W & Sharif M (1999) Stable expression of activated Ki-Ras does not constitutively activate the mitogen-activated protein kinase pathway but attenuates epidermal growth factor receptor activation in human astrocytoma cells. *Int J Oncol* 14(1):53-62.
22. Campbell PM*, et al.* (2007) K-Ras promotes growth transformation and invasion of immortalized human pancreatic cells by Raf and phosphatidylinositol 3-kinase signaling. *Cancer Res* 67(5):2098-2106.
23. Lim KH*, et al.* (2005) Activation of RalA is critical for Ras-induced tumorigenesis of human cells. *Cancer Cell* 7(6):533-545.
24. Lim KH*, et al.* (2006) Divergent roles for RalA and RalB in malignant growth of human pancreatic carcinoma cells. *Curr Biol* 16(24):2385-2394.
25. Zago G*, et al.* (2018) RalB directly triggers invasion downstream Ras by mobilizing the Wave complex. *Elife* 7.
26. Miller MJ*, et al.* (1997) RalGDS functions in Ras- and cAMP-mediated growth stimulation. *J Biol Chem* 272(9):5600-5605.
27. Apken LH & Oeckinghaus A (2021) The RAL signaling network: Cancer and beyond. *Int Rev Cell Mol Biol* 361:21-105.
28. Neel NF*, et al.* (2011) The RalGEF-Ral Effector Signaling Network: The Road Less Traveled for Anti-Ras Drug Discovery. *Genes Cancer* 2(3):275-287.
29. Huang L, Hofer F, Martin GS, & Kim SH (1998) Structural basis for the interaction of Ras with RalGDS. *Nat Struct Biol* 5(6):422-426.
30. Catozzi S, Halasz M, & Kiel C (2021) Predicted 'wiring landscape' of Ras-effector interactions in 29 human tissues. *NPJ Syst Biol Appl* 7(1):10.
31. Vigil D*, et al.* (2010) Aberrant overexpression of the Rgl2 Ral small GTPase-specific guanine nucleotide exchange factor promotes pancreatic cancer growth through Ral-dependent and Ral-independent mechanisms. *J Biol Chem* 285(45):34729-34740.
32. Emsley P, Lohkamp B, Scott WG, & Cowtan K (2010) Features and development of Coot. *Acta Crystallogr D Biol Crystallogr* 66(Pt 4):486-501.
33. Torices R & Munoz-Pajares AJ (2015) PHENIX: An R package to estimate a size-controlled phenotypic integration index. *Appl Plant Sci* 3(5).
34. Kiel C & Serrano L (2006) The ubiquitin domain superfold: structure-based sequence alignments and characterization of binding epitopes. *J Mol Biol* 355(4):821-844.
35. Esser D*, et al.* (1998) Structure determination of the Ras-binding domain of the Ral-specific guanine nucleotide exchange factor Rlf. *Biochemistry* 37(39):13453-13462.
36. Menyhard DK*, et al.* (2020) Structural impact of GTP binding on downstream KRAS signaling. *Chem Sci* 11(34):9272-9289.
37. Ito Y*, et al.* (1997) Regional polysterism in the GTP-bound form of the human c-Ha-Ras protein. *Biochemistry* 36(30):9109-9119.
38. Young G*, et al.* (2018) Quantitative mass imaging of single biological macromolecules. *Science* 360(6387):423-427.
39. Tran TH*, et al.* (2021) KRAS interaction with RAF1 RAS-binding domain and cysteine-rich domain provides insights into RAS-mediated RAF activation. *Nat Commun* 12(1):1176.
40. Pacold ME*, et al.* (2000) Crystal structure and functional analysis of Ras binding to its effector phosphoinositide 3-kinase gamma. *Cell* 103(6):931-943.

41. Bunney TD*, et al.* (2006) Structural and mechanistic insights into ras association domains of phospholipase C epsilon. *Mol Cell* 21(4):495-507.
42. Stieglitz B*, et al.* (2008) Novel type of Ras effector interaction established between tumour suppressor NORE1A and Ras switch II. *EMBO J* 27(14):1995-2005.
43. Eves BJ*, et al.* (2022) Structures of RGL1 RAS-Association Domain in Complex with KRAS and the Oncogenic G12V Mutant. *J Mol Biol* 434(9):167527.
44. Lee KY*, et al.* (2020) Two Distinct Structures of Membrane-Associated Homodimers of GTP- and GDP-Bound KRAS4B Revealed by Paramagnetic Relaxation Enhancement. *Angew Chem Int Ed Engl* 59(27):11037-11045.
45. Packer MR*, et al.* (2021) Raf promotes dimerization of the Ras G-domain with increased allosteric connections. *Proc Natl Acad Sci U S A* 118(10).
46. Ingolfsson HI*, et al.* (2022) Machine learning-driven multiscale modeling reveals lipid-dependent dynamics of RAS signaling proteins. *Proc Natl Acad Sci U S A* 119(1).
47. Lee KY*, et al.* (2021) Oncogenic KRAS G12D mutation promotes dimerization through a second, phosphatidylserine-dependent interface: a model for KRAS oligomerization. *Chem Sci* 12(38):12827-12837.
48. Jang H, Muratcioglu S, Gursoy A, Keskin O, & Nussinov R (2016) Membrane-associated Ras dimers are isoform-specific: K-Ras dimers differ from H-Ras dimers. *Biochem J* 473(12):1719-1732.
49. Sarkar-Banerjee S*, et al.* (2017) Spatiotemporal Analysis of K-Ras Plasma Membrane Interactions Reveals Multiple High Order Homo-oligomeric Complexes. *J Am Chem Soc* 139(38):13466-13475.
50. Prakash P*, et al.* (2017) Computational and biochemical characterization of two partially overlapping interfaces and multiple weak-affinity K-Ras dimers. *Sci Rep* 7:40109.
51. Muratcioglu S*, et al.* (2015) GTP-Dependent K-Ras Dimerization. *Structure* 23(7):1325-1335.
52. Andreadelis I*, et al.* (2022) Membrane Composition and Raf[CRD]-Membrane Attachment Are Driving Forces for K-Ras4B Dimer Stability. *J Phys Chem B* 126(7):1504-1519.
53. Ozdemir ES, Koester AM, & Nan X (2022) Ras Multimers on the Membrane: Many Ways for a Heart-to-Heart Conversation. *Genes (Basel)* 13(2).
54. Kessler D*, et al.* (2019) Drugging an undruggable pocket on KRAS. *Proc Natl Acad Sci U S A* 116(32):15823-15829.
55. Tran TH*, et al.* (2020) The small molecule BI-2852 induces a nonfunctional dimer of KRAS. *Proc Natl Acad Sci U S A* 117(7):3363-3364.
56. Prior IA, Muncke C, Parton RG, & Hancock JF (2003) Direct visualization of Ras proteins in spatially distinct cell surface microdomains. *J Cell Biol* 160(2):165-170.
57. Weise K*, et al.* (2011) Membrane-mediated induction and sorting of K-Ras microdomain signaling platforms. *J Am Chem Soc* 133(4):880-887.
58. Lakshman B*, et al.* (2019) Quantitative biophysical analysis defines key components modulating recruitment of the GTPase KRAS to the plasma membrane. *J Biol Chem* 294(6):2193-2207.
59. Plowman SJ, Muncke C, Parton RG, & Hancock JF (2005) H-ras, K-ras, and inner plasma membrane raft proteins operate in nanoclusters with differential dependence on the actin cytoskeleton. *Proc Natl Acad Sci U S A* 102(43):15500-15505.

60. Zhou Y*, et al.* (2014) Signal integration by lipid-mediated spatial cross talk between Ras nanoclusters. *Mol Cell Biol* 34(5):862-876.
61. Pai EF*, et al.* (1990) Refined crystal structure of the triphosphate conformation of H-ras p21 at 1.35 A resolution: implications for the mechanism of GTP hydrolysis. *EMBO J* 9(8):2351-2359.
62. Kapust RB*, et al.* (2001) Tobacco etch virus protease: mechanism of autolysis and rational design of stable mutants with wild-type catalytic proficiency. *Protein Eng* 14(12):993-1000.
63. Tropea JE, Cherry S, & Waugh DS (2009) Expression and purification of soluble His(6)-tagged TEV protease. *Methods Mol Biol* 498:297-307.
64. Smith SJ & Rittinger K (2002) Preparation of GTPases for structural and biophysical analysis. *Methods Mol Biol* 189:13-24.
65. Evans PR & Murshudov GN (2013) How good are my data and what is the resolution? *Acta Crystallogr D Biol Crystallogr* 69(Pt 7):1204-1214.
66. McCoy AJ*, et al.* (2007) Phaser crystallographic software. *J Appl Crystallogr* 40(Pt 4):658-674.
67. Murshudov GN*, et al.* (2011) REFMAC5 for the refinement of macromolecular crystal structures. *Acta Crystallogr D Biol Crystallogr* 67(Pt 4):355-367.
68. Joosten RP, Long F, Murshudov GN, & Perrakis A (2014) The PDB_REDO server for macromolecular structure model optimization. *IUCrJ* 1(Pt 4):213-220.
69. Boucher W (Azara, v2.7 http://www.bio.cam.ac.uk/azara/.
70. Hamatsu J*, et al.* (2013) High-resolution heteronuclear multidimensional NMR of proteins in living insect cells using a baculovirus protein expression system. *J. Am. Chem. Soc.* 135(5):1688-1691.
71. Vranken WF*, et al.* (2005) The CCPN data model for NMR spectroscopy: development of a software pipeline. *Proteins* 59(4):687-696.
72. Güntert P & Buchner L (2015) Combined automated NOE assignment and structure calculation with CYANA. *J. Biomol. NMR* 62(4):453-471.
73. Wallace AC, Laskowski RA, & Thornton JM (1995) LIGPLOT: a program to generate schematic diagrams of protein-ligand interactions. *Protein Eng* 8(2):127-134.

Figures and Tables

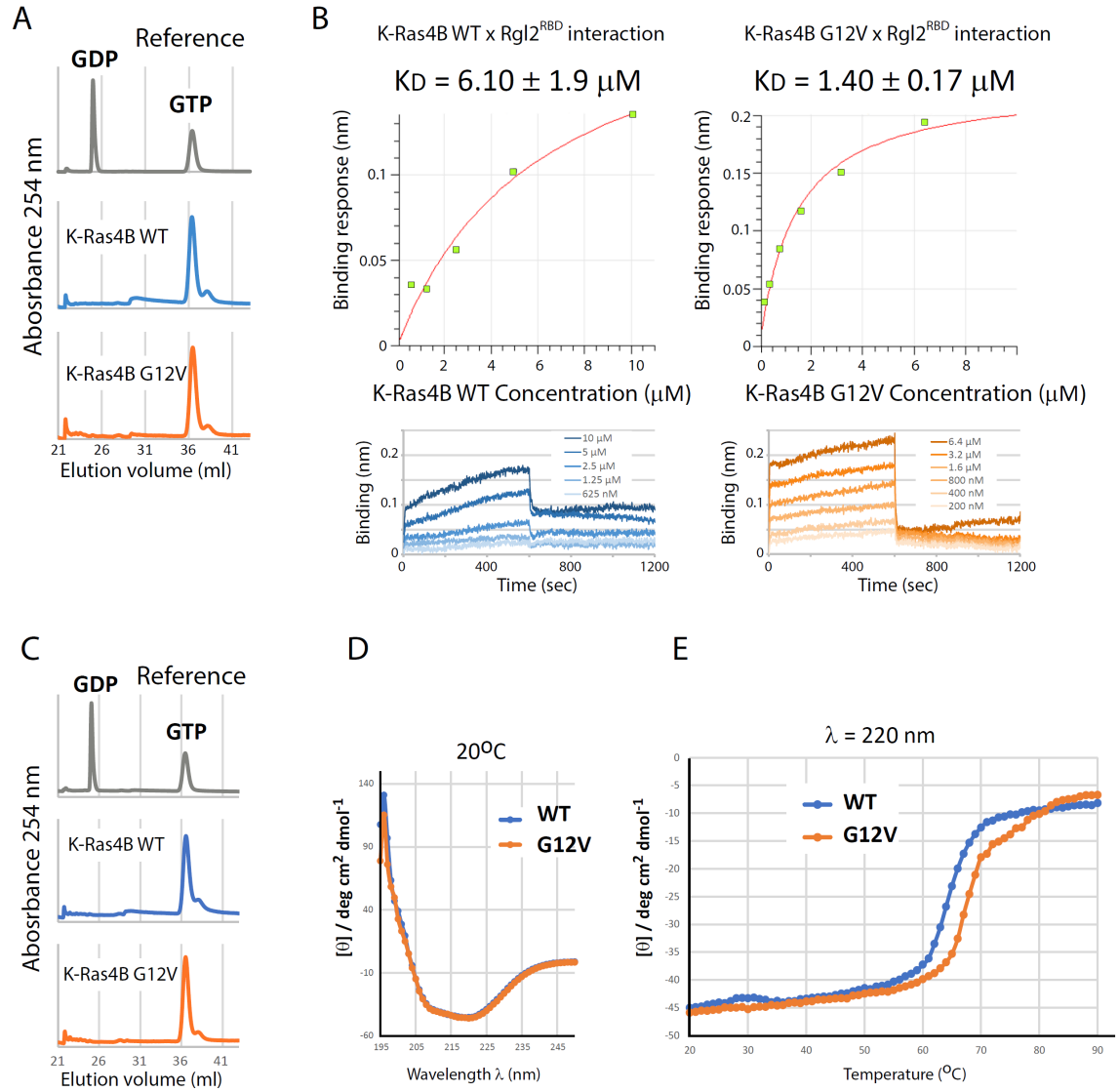

Figure 1. K-Ras4B^{G12V} is structurally more stable and has a stronger affinity towards Rgl2^{RBD} than K-Ras4B^{WT}.

Analyses of binding kinetics of GST-Rgl2^{RBD} and K-Ras4B^{WT} or K-Ras4B^{G12V}. Biolayer Interferometry (BLI) was used to directly measure the steady state binding of K-Ras4B (analyte) to immobilized GST-Rgl2^{RBD} (ligand). (A and C) K-Ras4B^{WT} and K-Ras4B^{G12V} samples used for BLI and Circular Dichroism (CD) were confirmed to be fully loaded with GTP. The nucleotide binding status of K-Ras4B^{WT} and K-Ras4B^{G12V} were examined by denaturating the proteins and detecting

the released nucleotides by anion exchange chromatography. Samples of pure GDP or GTP were used as references. (B) BLI results of binding between K-Ras4B^{WT}/K-Ras4B^{G12V} and Rgl2^{RBD}. GST-Rgl2^{RBD} was immobilised on the bio-sensors, and varying concentrations of free K-Ras4B^{WT} (left panels) and K-Ras4B^{G12V} (right panels) were provided and the interactions were measured at 23°C. The kinetics diagrams (lower panels, association at t=0(s), dissociation at t=300(s)) revealed a fast on/off binding. Therefore, steady state curves (upper panels) were used to estimate the K_D values; about 6.1 µM for K-Ras4B^{WT}:Rgl2^{RBD} and 1.4 µM for K-Ras4B^{G12V}:Rgl2^{RBD}, respectively. (D) Circular dichroism (CD) spectra of K-Ras4B^{WT} and K-Ras4B^{G12V} at 20°C. (E) CD signal intensity at 220 nm as a function of temperature from 20°C to 90°C.

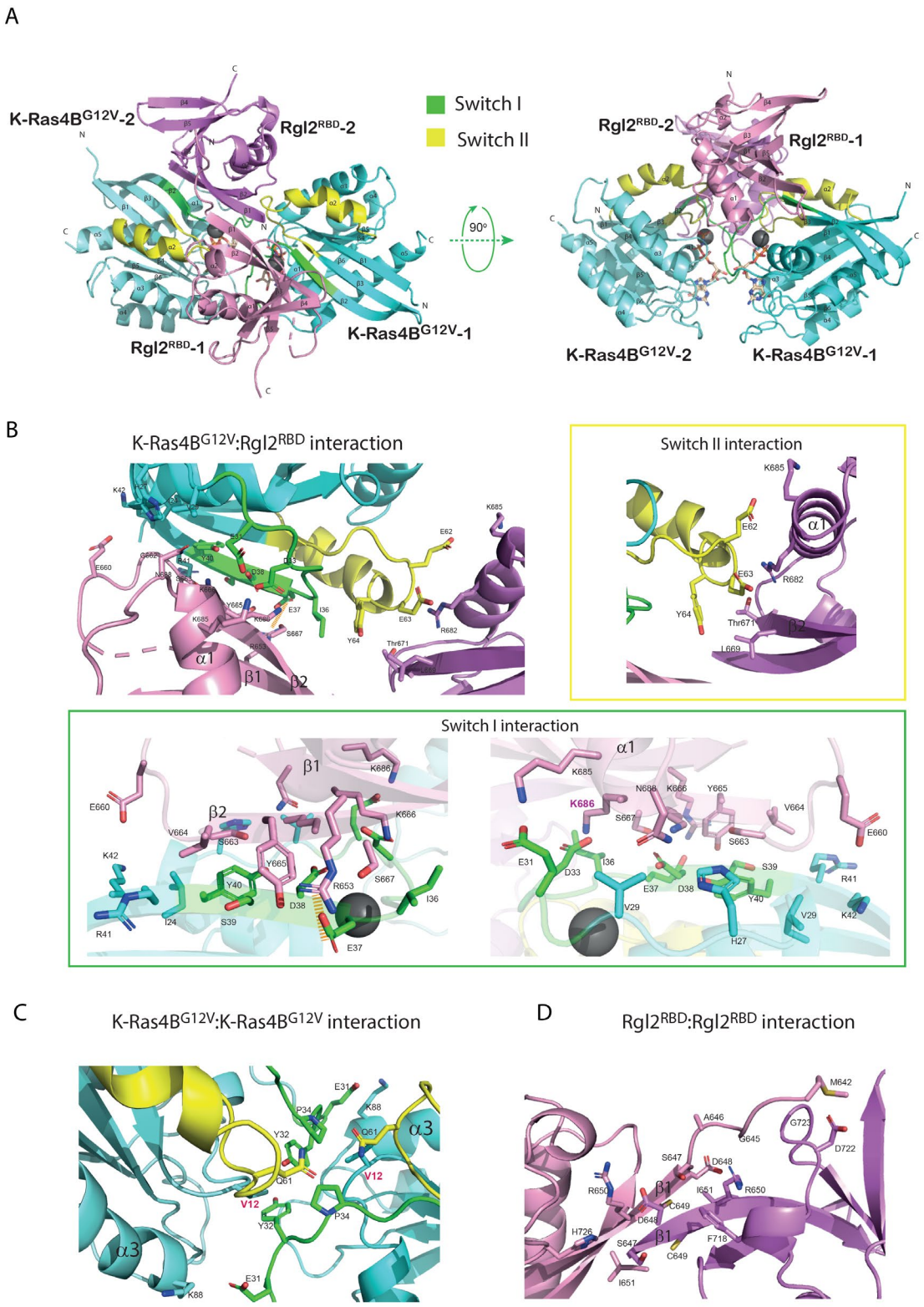

Figure 2. Crystal structure of the K-Ras4B^{G12V}:Rgl2^{RBD} 2:2 heterotetramer

(A) Cartoon representation of the structure of the heterotetramer complex of K-Ras4B^{G12V} and Rgl2^{RBD} with top view and side view; the two K-Ras4B^{G12V} molecules are shown in dark and pale cyan and the two molecules of Rgl2^{RBD} in pink and violet. Switch-I and Switch-II regions of K-Ras4B^{G12V} are shown in green and yellow, respectively, and the α-helix and β-sheets are numbered for each chain. The Mg^{2+} is shown as a grey sphere. The structure shows that each K-Ras4B^{G12V} molecule interacts with two Rgl2^{RBD} molecules (referred to as 1 and 2) at Switch-I and Switch-II individually. (B) The interacting interface of K-Ras4B^{G12V} and Rgl2^{RBD}, highlighting the residues involved in hydrogen and hydrophobic interactions between β1, β2 and α1 of Rgl2^{RBD1} (violet sticks) and K-Ras4B^{G12V} Switch-I (green sticks, enlarged in the green box) or Switch-II (yellow sticks, enlarged in the yellow box). An orange dotted line shows a salt bridge formed between E37 of K-Ras4B^{G12V} and R653 of Rgl2^{RBD}. K686 of Rgl2^{RBD}, which plays an essential role in the complex formation as shown in Supplementary Fig. S5, is annotated in purple letters. (C) The interacting interface of K-Ras4B^{G12V}: K-Ras4B^{G12V}, highlighting the residues involved in hydrogen and hydrophobic interactions between two K-Ras4B^{G12V} molecules. The interface comprises Switch-I, Switch-II and α3 of the two K-Ras4B^{G12V} molecules. The oncogenic mutation, V12, is annotated in red letters. (D) The interacting interface of Rgl2^{RBD}: Rgl2^{RBD}, highlighting the residues involved in hydrogen and hydrophobic interactions between two Rgl2^{RBD} molecules, shaded in pink and violet. The interaction occurs at the N-terminal between the two anti-parallel β1.

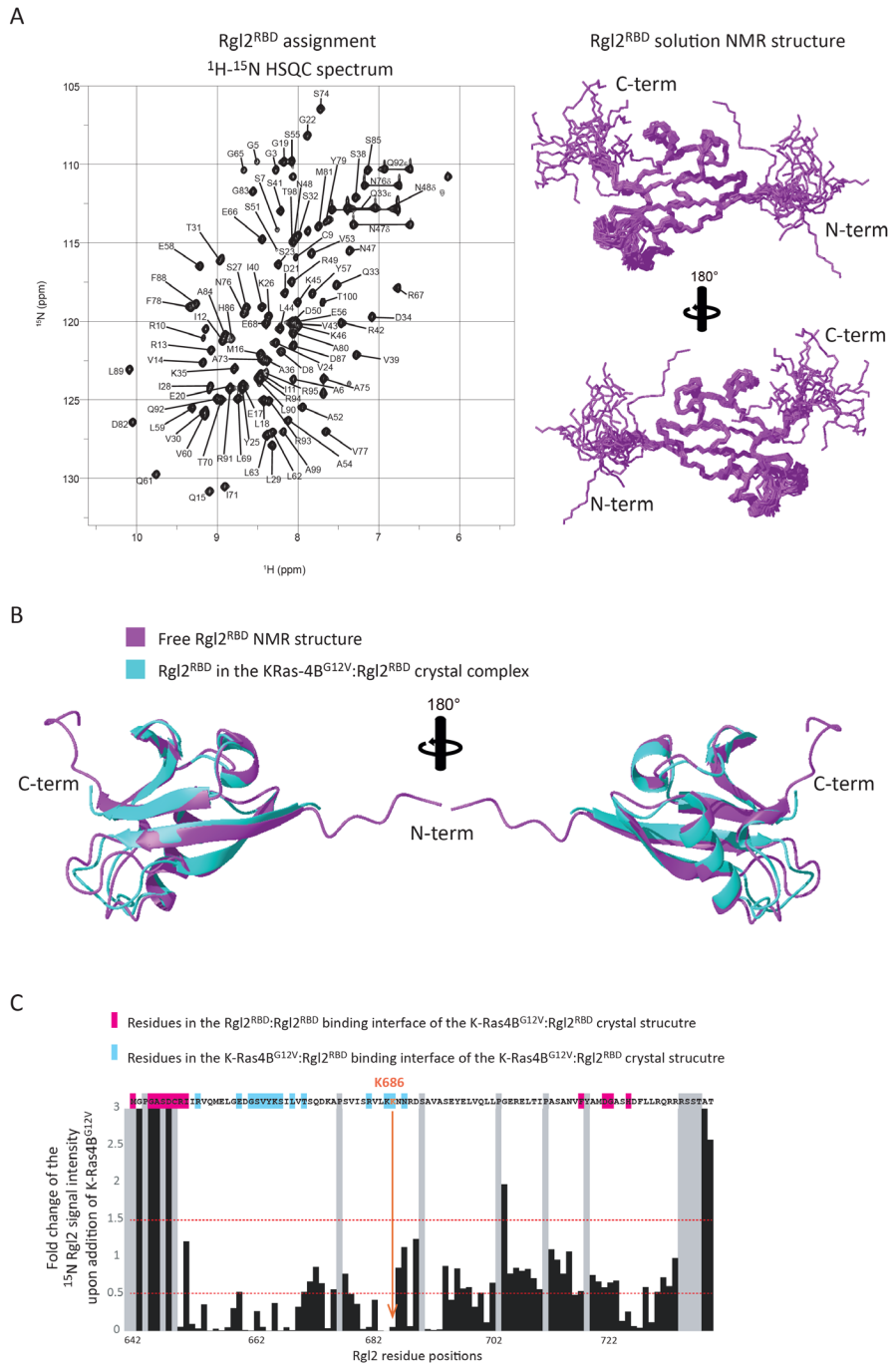

Figure 3. NMR analysis of K-Ras4B^{G12V}:Rgl2^{RBD} complex formation in solution

(A) Rgl2^{RBD} solution structure determined by NMR. The 2D ^{1}H-^{15}N-HSQC spectrum of the assigned residues of the Rgl2^{RBD} is shown (left). The Rgl2^{RBD} retains the ββαββαβ ubiquitin-fold structure (right). 20 Rgl2 NMR structures are superimposed. (B) Comparison between the Rgl2^{RBD}

structures identified in solution NMR (shown in magenta) and in crystal complex with K-Ras4B^{G12V} (shown in cyan). (C) NMR signal intensity changes of ^{15}N-labelled Rgl2^{RBD} upon addition of non-labelled K-Ras4B^{G12V} as a function of Rgl2^{RBD} amino acid sequence. The original HSQC spectra of the titration experiment are presented in Supplementary Fig. S4B. The signal intensities of Rgl2^{RBD} residues in the presence of three times molar excess of K-Ras4B^{G12V} were divided by the signal intensities in the absence of K-Ras4B^{G12V} and plotted as a bar-chart graph. Proline and unassigned Rgl2^{RBD} residues are shaded in grey. Red-dotted lines are drawn at the fold-change values of 0.5 and 1.5 to highlight the residues that show substantial increase or decrease of the signals upon addition of K-Ras4B^{G12V}. Rgl2^{RBD} residues involved in the Rgl2^{RBD}:Rgl2^{RBD} interface of the K-Ras4B^{G12V}:Rgl2^{RBD} crystal structure are highlighted in pink on the amino acid sequence, and residues involved in the K-Ras4B^{G12V}:Rgl2^{RBD} interface are highlighted in blue. Rgl2^{RBD} residue position numbers according to the UniProt are indicated at the bottom of the diagram. K686, which plays a crucial role in the K-Ras4B^{G12V} complex formation, is annotated in orange.

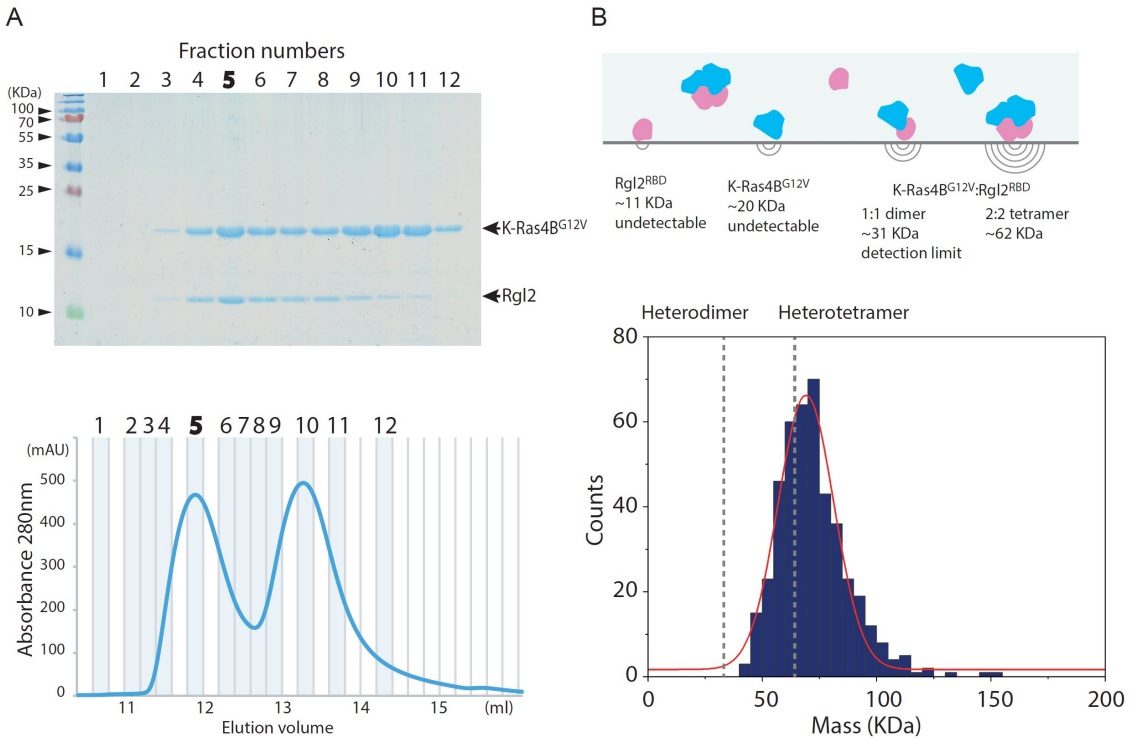

Figure 4. K-Ras4B^{G12V}:Rgl2^{RBD} complex can form a heterotetramer in solution

Mass photometry analysis of KRas4B^{G12V}:Rgl2^{RBD} complex in solution. (A) K-Ras4B^{G12V}:Rgl2^{RBD} complex was purified using size exclusion chromatography. The fractions were analysed by 15% SDS-PAGE gel (upper panel) according to the elution profile (lower panel). Fraction 5 was chosen and diluted to a concentration of 40nM for measurement using mass photometry (OneMP, Refeyn). (B) Cartoon representing the different complexes configurations possibilities indicating that only heterodimers (~31kDa) and heterotetramers (~62kDa) can be detected the system. Histogram of the frequency counts against of the purified KRas4B^{GV}:Rgl2^{RBD} complex with fitting for Gaussian distribution (red). The duration of the video analysed was 60s and it shows that the population identified has an average mass of ~68kDa, which is in good agreement with the expected MW of the heterotetramer (61.7kDa).

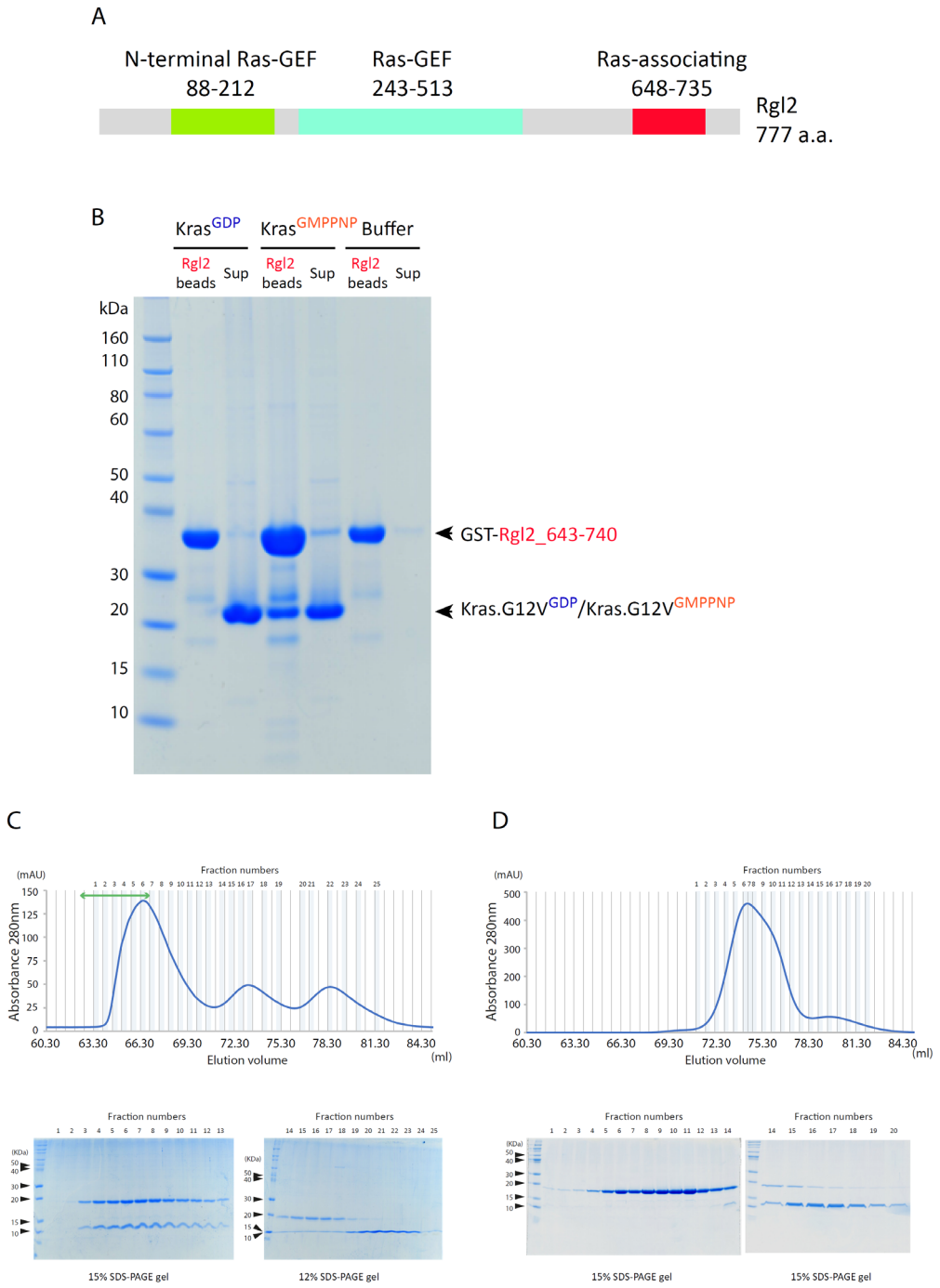

Figure S1. Rgl2 Ras binding domain interacts with active K-Ras4B^{G12V}.

(A) A schematic diagram of domains organization of human Rgl2 as defined in the UniProt database (Uniprot number: O15211). A domain spanning amino acid residues 648-735 is annotated as "Ras-associating" by PROSITE annotation rule PRU00166. In this work, we

generically call this domain Rgl2 Ras Binding Domain ($Rgl2^{RBD}$). (B) $Rgl2^{RBD}$ interacts with active K-$Ras4B^{G12V}$. Bacteria recombinant $Rgl2^{RBD}$ fragment spanning the amino acid residues 643-740 of Rgl2 was fused with GST and the fusion protein was fixed on glutathione beads. Recombinant K-$Ras4B^{G12V}$ 1-169, loaded with either GDP or non-hydrolisable GTP analogue, GMPPNP, was applied on the beads to examine the protein-protein interaction. GST-$Rgl2^{RBD}$ interacted only with the GMPPNP-loaded K-$Ras4B^{G12V}$. (C) .K-$Ras4B^{G12V}$:$Rgl2^{RBD}$ complex was purified using size exclusion chromatography. The fractions were analyzed by 15% or 12% SDS-PAGE gel (lower panel) according to the elution profile (upper panel). Fractions indicated by the green double-arrow line were used for crystallization trials. (D) K-$Ras4B^{WT}$ and $Rgl2^{RBD}$ preparations were mixed and applied to size exclusion chromatography. The elution profile (upper panel) shows little complex formation. Peak fractions were analyzed by 15% SDS-PAGE gel (lower panel).

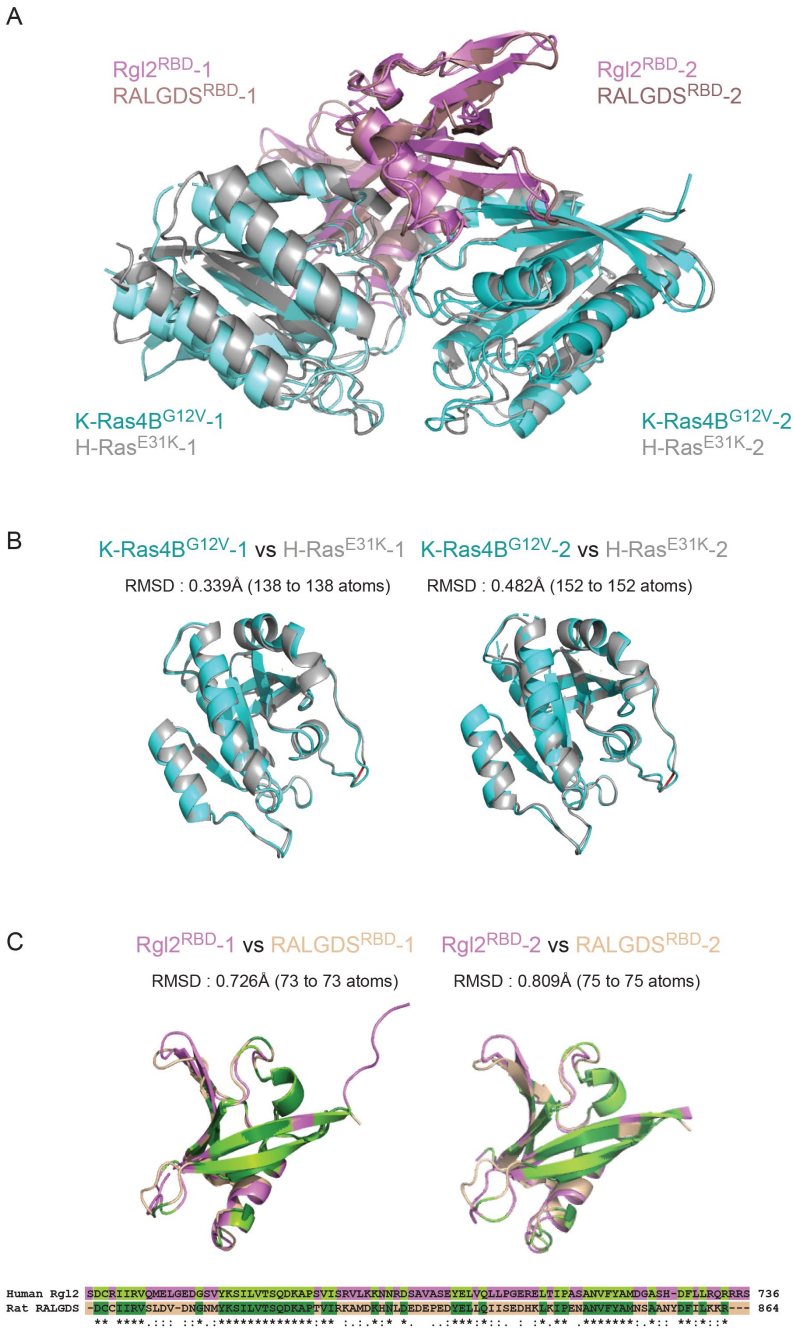

Figure S2. K-Ras4B^{G12V}:Rgl2^{RBD} complex is highly similar to H-Ras^{E31K}:RALGDS^{RBD} complex

(A) The structures of the K-Ras4B^{G12V}:Rgl2^{RBD} complex and the H-Ras^{E31K}:RALGDS^{RBD} complex (PDB: 1LFD) were superimposed by aligning the RBD chains. (B) and (C) Superimposition of each corresponding chain of the K-Ras4B^{G12V}: Rgl2^{RBD} complex and H-Ras^{E31K}:RALGDS^{RBD} complex

individually shows that each chain is similar to its respective counterpart structure. (B) K-Ras4B^{G12V} and H-Ras^{E31K} chains are in cyan and grey. (C) Rgl2^{RBD} and RALGDS^{RBD} are in purple and light pink. Amino acid sequence similarities of human Rgl2^{RBD} and rat RALGDS^{RBD} are shown below the RBD cartoon representations, and the conserved amino acids in Rgl2^{RBD} and RALGDS^{RBD} are shaded in light green and dark green, respectively. The structural similarity between Rgl2^{RBD} and RALGDS^{RBD} was seen beyond the regions composed of the conserved amino acids. The RALGDS^{RBD} sequence is derived from PDB 1LFD, which is rat RALGDS^{RBD}, and the numbering was done according to Uniprot Q03386. Root-mean-square deviation of atomic positions (RMSD) values were generated using Pymol.

A

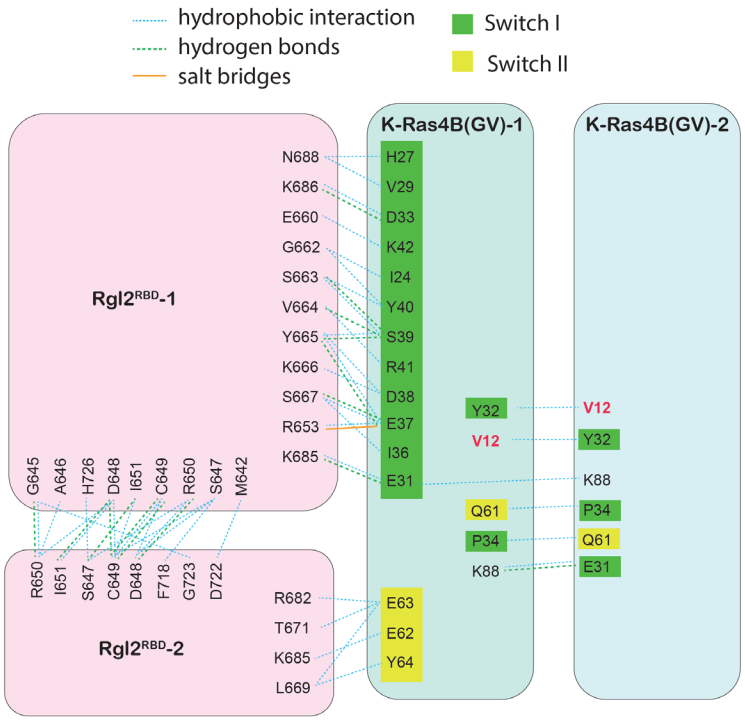

B

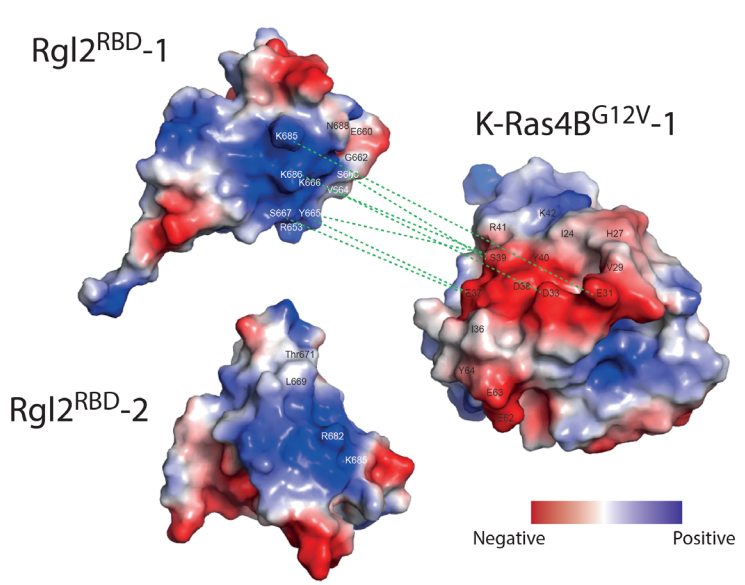

Figure S3. Schematic representation of the intermolecular contacts observed in the X-ray structure

(A) The residues in K-Ras4B^{G12V} Switch-I region are shown in green, in the Switch-II region are shown in yellow background and those for Rgl2^{RBD} molecules 1 and 2 are shown in pink. V12 oncogenic mutation is in red. Hydrogen bonds, salt bridges and hydrophobic interactions were predicted by LIGPLOT and represented by green dashed lines, solid orange lines and blue dotted lines, respectively. (B) The electrostatic surface charge shows that the negatively charged Switch-I and Switch-II regions of KRas4B^{GV} interact with the positively charged surface of Rgl2^{RBD}-1 and Rgl2^{RBD}-2. Surface charge potential was computed using the Pymol vacuum electrostatics function, and the negatively charged and positively charged areas are shown in red and blue, respectively.

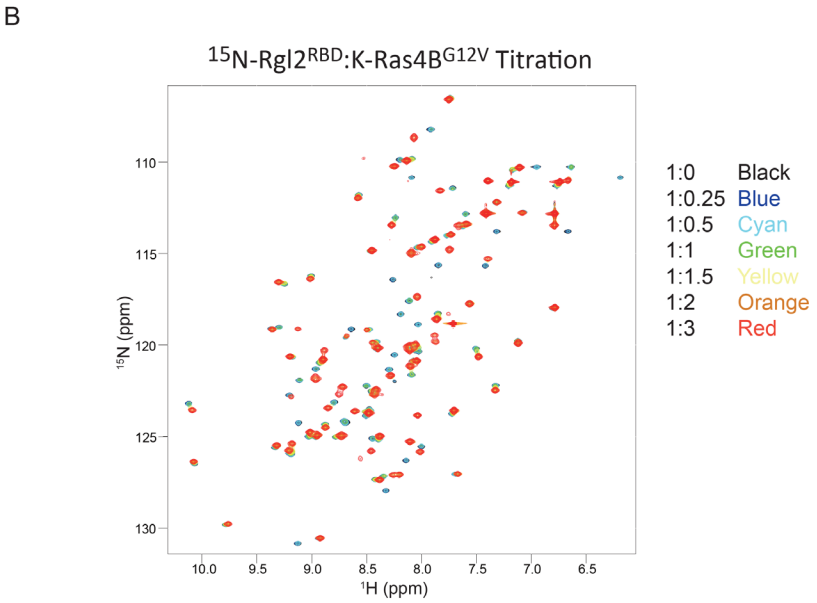

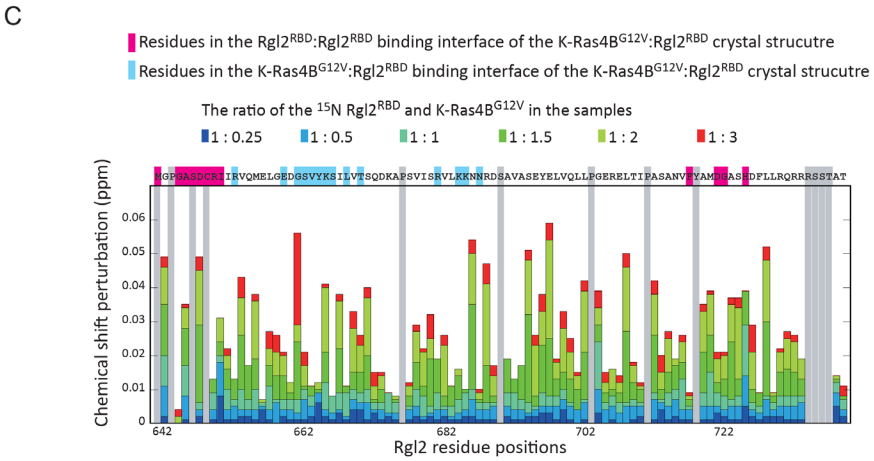

Figure S4. K-Ras4B^{G12V}:Rgl2^{RBD} complex formation in solution

(A) Comparison between the human $Rgl2^{RBD}$ and mouse Rlf^{RBD} (PDB 1RLF) solution structures. $Rgl2^{RBD}$ is presented in magenta, and 20 NMR structures are superimposed. Rlf^{RBD} is in cyan, and 10 NMR structures are superimposed. The primary structures of the two constructs are listed below. (B) and (C) ^{1}H-^{15}N HSQC titration analysis of ^{15}N-labelled $Rgl2^{RBD}$ upon addition of non-labelled K-Ras4B^{G12V} supports the K-Ras4B^{G12V}:$Rgl2^{RBD}$ tetramer formation. (B) Overlays of 2D ^{1}H-^{15}N HSQC NMR spectra from multipoint titrations of ^{15}N-labelled $Rgl2^{RBD}$ with non-labelled K-Ras4B^{G12V}.. $Rgl2^{RBD}$:K-Ras4B^{G12V} molar ratios of the titration samples are colour-coded as follows; 1:0 - black, 1:0.25 - blue, 1:0.25 – cyan, 1:0.5 – green, 1:1 – yellow, 1:2 – orange and 1:3 – red. (C) The chemical shift perturbation of backbone $^{1}H^{N}$ and ^{15}N nuclei of $Rgl2^{RBD}$ with non-labelled K-Ras4B^{G12V}, presented in (B), is summarised as a column diagram. The mean shift difference $\Delta\delta_{ave}$ was calculated as $[(\Delta\delta^{1}H^{N})^{2} + (\Delta\delta^{15}N/10)^{2}]^{1/2}$ where $\Delta\delta^{1}H^{N}$ and $\Delta\delta^{15}N$ are the chemical shift differences between $Rgl2^{RBD}$ on its own and in the presence of non-labelled K-Ras4B^{G12V}. The bar graphs are colour-coded according to the $Rgl2^{RBD}$- K-Ras4B^{G12V} concentration ratio and are overlaid. Proline and unassigned residues are shaded in grey. $Rgl2^{RBD}$ residues in the $Rgl2^{RBD}$:$Rgl2^{RBD}$ interface of the K-Ras4B^{G12V}:$Rgl2^{RBD}$ crystal structure is highlighted in pink and residues in the K-Ras4B^{G12V}:$Rgl2^{RBD}$ interface of the crystal structure is highlighted in blue. $Rgl2^{RBD}$ residue positions according to the UniProt are indicated at the bottom of the diagram.

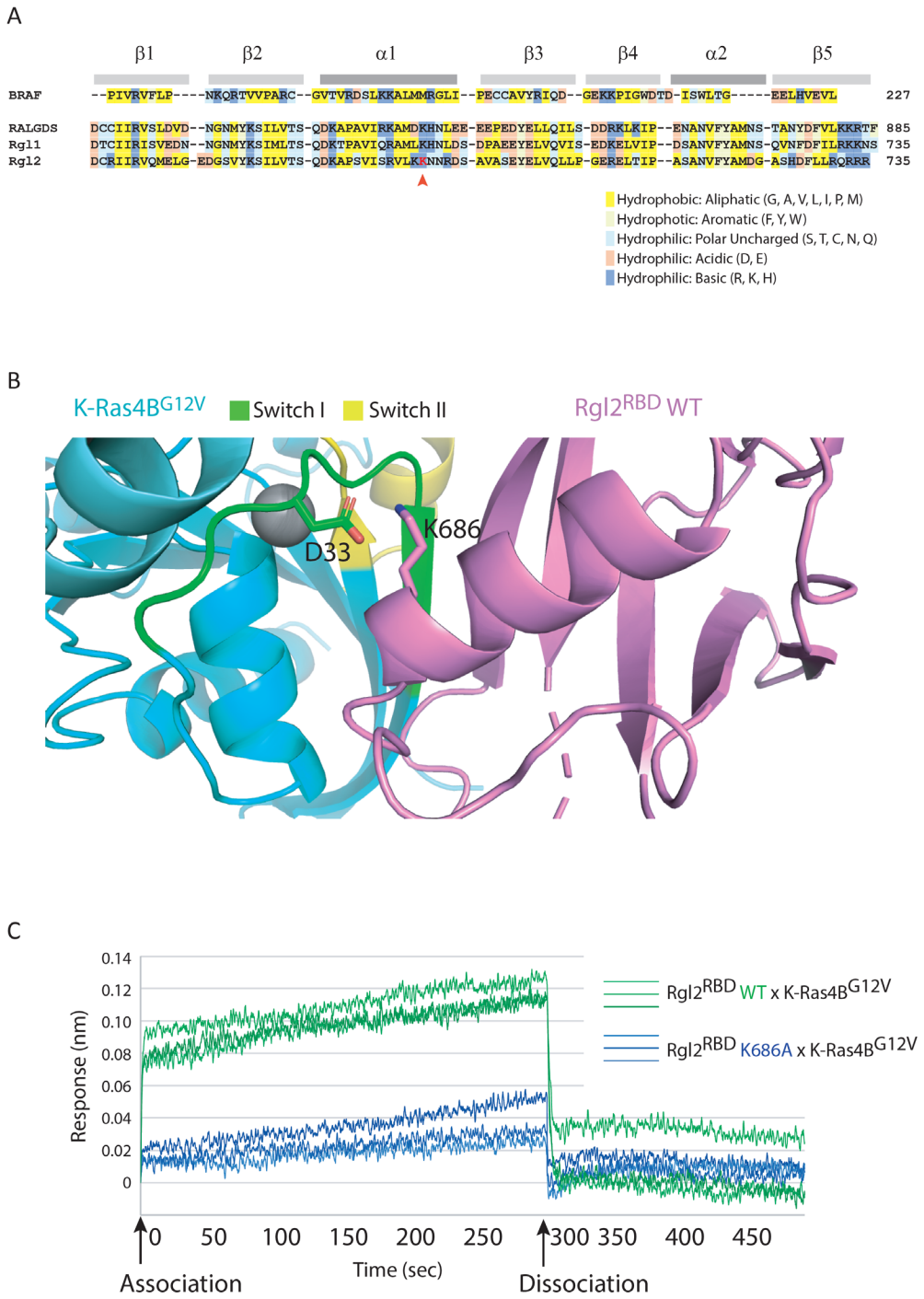

Figure S5. Rgl2 K686 plays a key role in the complex formation

(A) Multiple sequence alignment of Ras binding domain (RBD) of human BRAF (residues 155-227) and Ras Associating (RA) domains of human RALGDS (residues 798-885), Rgl1 (residues

648-735) and Rgl2 (residues 648-735), as defined by UniProt. The alignment reveals that sequences are relatively divergent between BRaf^{RBD} and RalGDS family, although all RBD/RA domains share the common ubiquitin fold ββαββαβstructure. The RalGDS family shares a high degree of sequence homology, including the red-arrowhead-indicated key lysine 686 residue (highlighted in red, K686 in Rgl2^{RBD}), which is involved in the Ras:RA complex interface. **(B)** The conserved K686 residue in Rgl2^{RBD} interacts via a hydrogen bond and hydrophobic interaction with D33 in the Switch-I region of KRas4B^{G12V}. **(D)** Rgl2^{RBD}-K686A mutant hinders the interaction between Rgl2^{RBD} and KRas4B. The Biolayer interferometry analysis of Rgl2^{RBD}-K686A mutant and KRas4B^{G12V} did not give a conclusive Kd, likely due limitation of the technique in measuring low binding affinity. The reduced affinity of the K686A mutant can be illustrated by a comparison between Rgl2^{RBD}-K686A mutant and Rgl2^{RBD}-WT amplitudes during the association step with KRas4B^{G12V}, which shows a decrease in the case of K686A mutant.

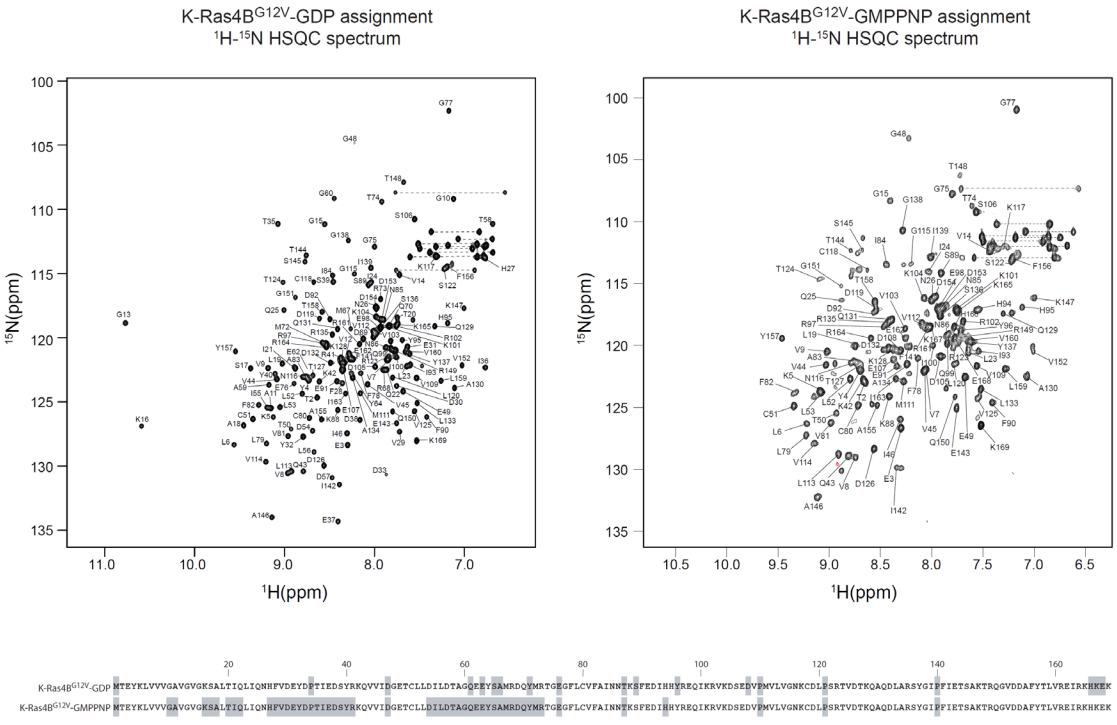

Figure S6. Backbone resonance assignment of GDP-bound and GMPPNP-bound K-Ras4B^{G12V}

The 2D ^{1}H-^{15}N-HSQC spectra of GDP-Bound and GMPPNP-bound K-Ras4B^{G12V}. Cross peaks are labelled with their corresponding backbone assignments. Residues which could not be assigned are shaded in grey in the primary sequence shown at the bottom.

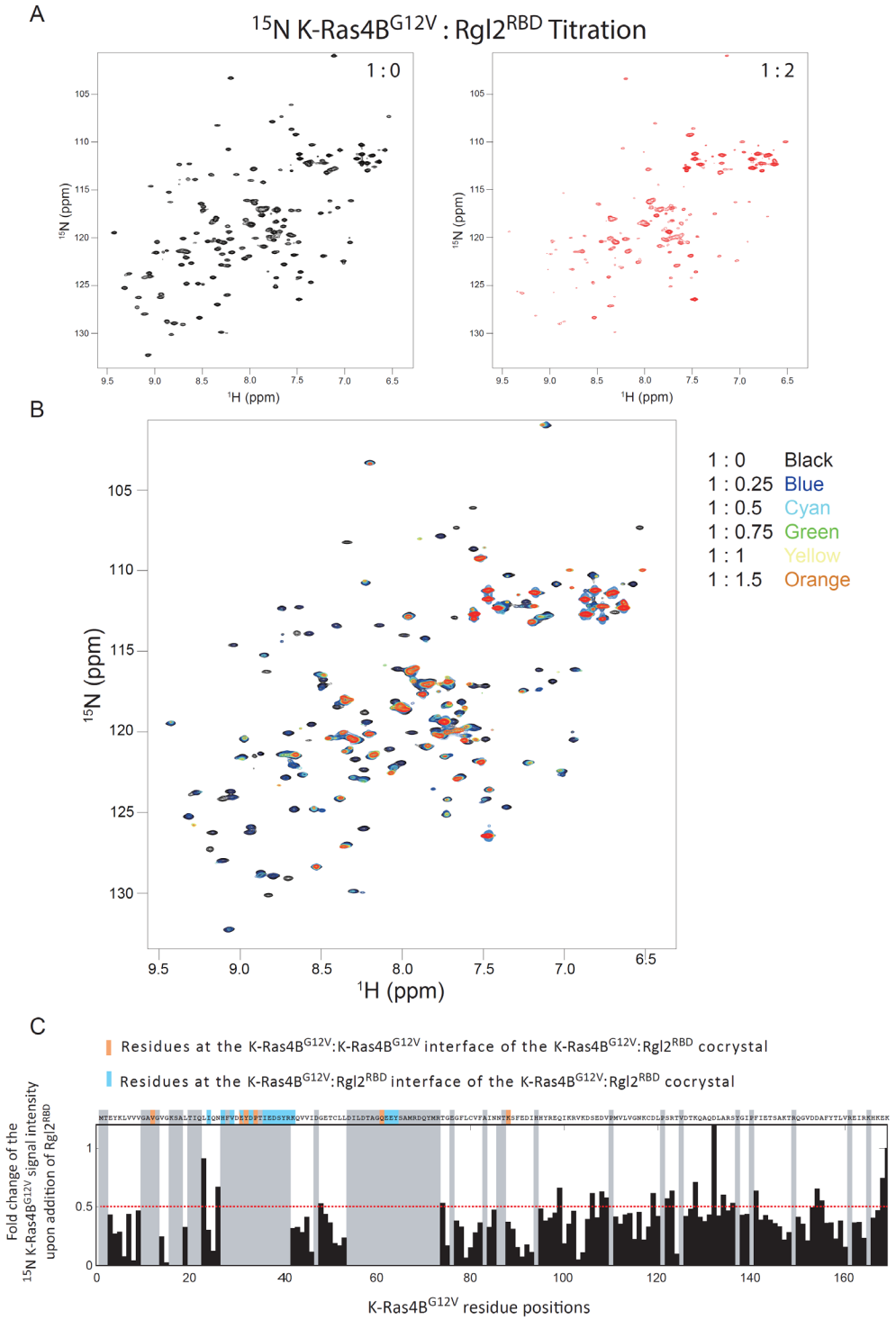

Figure S7. K-Ras4B^{G12V}:Rgl2^{RBD} complex formation in solution

^{1}H-^{15}N-HSQC titration analysis of ^{15}N-labelled K-Ras4B^{G12V} upon addition of non-labelled Rgl2^{RBD} supports the K-Ras4B^{G12V}:Rgl2^{RBD} tetramer formation. (A) and (B) The 2D ^{1}H-^{15}N-HSQC NMR spectra of K-Ras4B^{G12V}. ^{15}N-labelled K-Ras4B^{G12V} was titrated with non-labelled Rgl2^{RBD}. (A) The 2D ^{1}H-^{15}N-HSQC spectra of K-Ras4B^{G12V}: Rgl2^{RBD} complex mixed with the molar ratio of 1:0 (black, left panel) and 1:2 (red, right panel) are shown. Many signals from ^{15}K-Ras4B^{G12V} residues disappeared upon the addition of Rgl2^{RBD}. (B) Superimposed 2D ^{1}H-^{15}N-HSQC NMR spectra of ^{15}N-labelled K-Ras4B^{G12V}:Rgl2^{RBD} titration experiments. The titration samples are colour-coded as follows; 1:0-black, 1:0.25 - blue, 1:0. 5 – cyan, 1:0.75 –green, 1:1 – yellow, 1:1.5 – orange and 1:2 – red. (C) Fold changes of the signal intensities of ^{15}N-labelled K-Ras4B^{G12V} upon addition of non-labelled Rgl2^{RBD}. The signal intensities of K-Ras4B^{G12V} residues in the presence of two times molar excess of Rgl2^{RBD} were divided by the signal intensities in the absence of Rgl2^{RBD}, and the obtained values were plotted as a column graph. Undetectable residues are shaded in grey. The residue T2 was also shaded grey, as the chemical shift after the addition of Rgl2^{RBD} overlapped with other signals. A red-dotted line is drawn at the fold-change values of 0.5 to indicate that the most residues show substantial decrease of the signals upon addition of Rgl2^{RBD}. K-Ras4B^{G12V} residues in the K-Ras4B^{G12V}: K-Ras4B^{G12V} interface of the K-Ras4B^{G12V}:Rgl2^{RBD} crystal structure is highlighted in orange, and residues in the K-Ras4B^{G12V}:Rgl2^{RBD} interface of the crystal structure is highlighted in blue. K-Ras4B^{G12V} residue positions according to the UniProt are indicated at the bottom of the diagram.

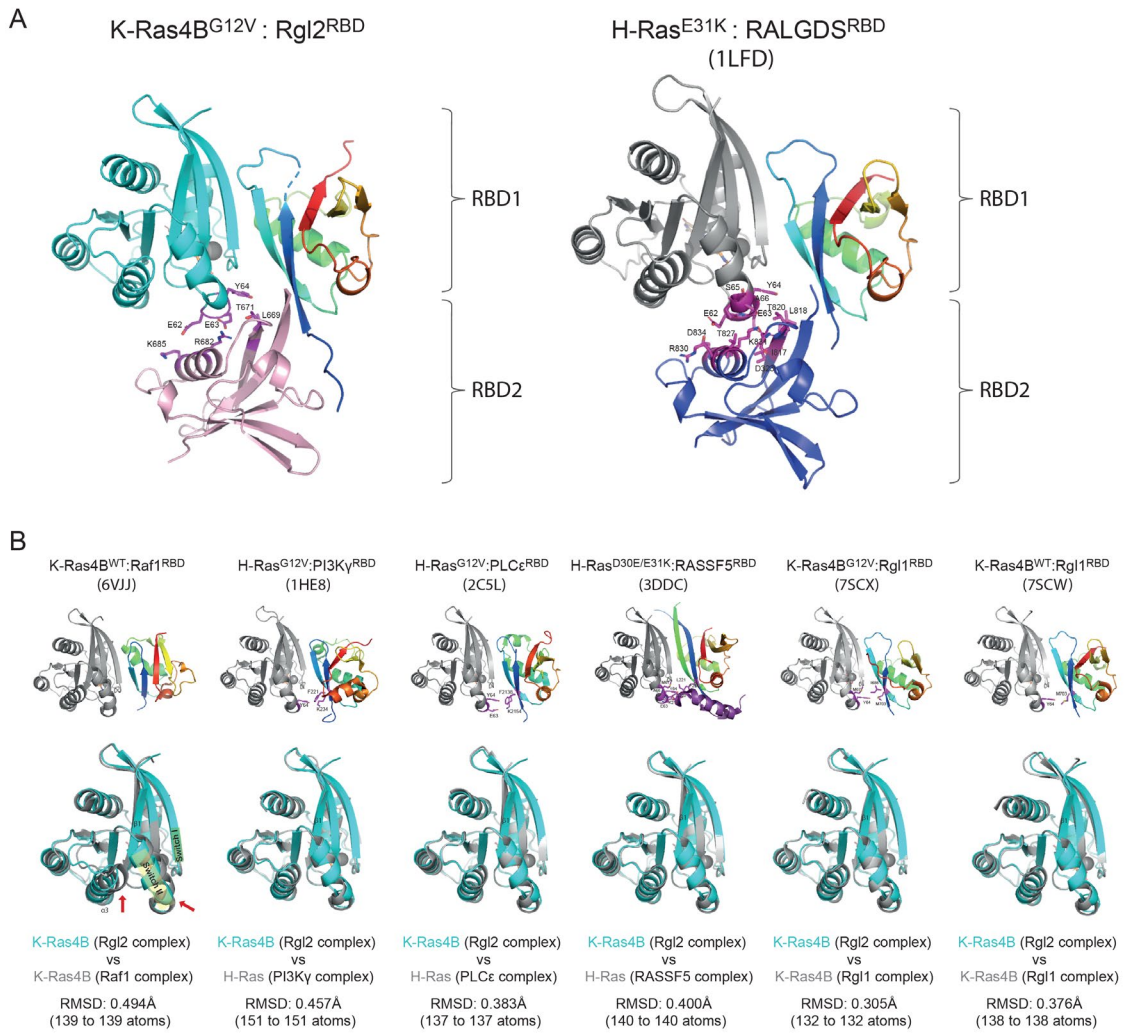

Figure S8. Ras:RalGEF^{RBD} complex formation is distinct from other Ras:effector complexes.

K-Ras4B^{G12V}:Rgl2^{RBD} complex was compared with representative Ras:effector complexes. The spectrum colour feature illustrates the orientation and ubiquitin super-fold status for one of the RBD(s). When two RBDs interact with one Ras molecule, the second RBD is coloured pink (Rgl2^{RBD}) or blue (RALGDS^{RBD}). The K-Ras4B^{G12V} in the Rgl2^{RBD} complex is in cyan, and other Ras molecules from previously published structures are in grey. The interacting residues involved in Ras Switch-II and RBDs are depicted with magenta sticks and are labelled. (A) The two Ras:RalGEF complexes (K-Ras4B^{G12V}:Rgl2^{RBD} complex and H-Ras^{E31K}:RALGDS^{RBD} complex PDB: 1LFD) show similar structural features, including the orientation of the RBDs, the Switch-I contact and the mode of usage of Switch-II. Two RBDs (RBD-1 in the spectrum colour and RBD-2

in either pink or in blue) interact separately with a single Ras molecule at Switch-I and Switch-II regions. (B) Examples of Ras:effector complex crystal structures. K-Ras4B^{WT}:Raf1 complex (PDB: 6VJJ) shows that although Raf1^{RBD} has similar orientations of the ubiquitin fold structure to Rgl2^{RBD}-1, it does not utilise Ras Switch-II in complex formation. Superimposition of the K-Ras4B^{G12V} of the Rgl2^{RBD} complex onto the K-Ras4B^{WT} of the Raf1^{RBD} complex shows some differences in Switch-II, β1 and α3 (arrows). PI3Kγ^{RBD} (PDB:1HE8) and PLCε^{RBD} (PDB:2C5L) complexed with Ras utilise Switch-II region differently to Ras:RalGEF complexes despite a similar orientation of the ubiquitin fold structure of RBDs. A single RBD interacts at both Switch-I and Switch-II regions of one Ras molecule. Superimposed H-Ras molecules in these complexes to K-Ras4B^{G12V} in the Rgl2^{RBD} complex gave lower RMSD values compared to K-Ras4B^{WT} in the Raf1^{RBD} complex. H-Ras$^{D30E/E31K}$:RASSF5^{RBD} complex (3DDC) shows yet another unique interaction where the additional α-helix at the N-terminal of the RBD interacts with the Switch-II region of the Ras molecule, instead of the RBD region itself. Rgl1 is one of the RalGEFs, as Rgl2 and RALGDS are. However, unlike Rgl2 or RALGDS, K-Ras4B^{G12V}:Rgl1^{RBD} complex (7SCX) and K-Ras4B^{WT}:Rgl1^{RBD} complex (7SCW) show one Rgl1^{RBD} to interact with both Switch-I and Switch-II of one Ras molecule.

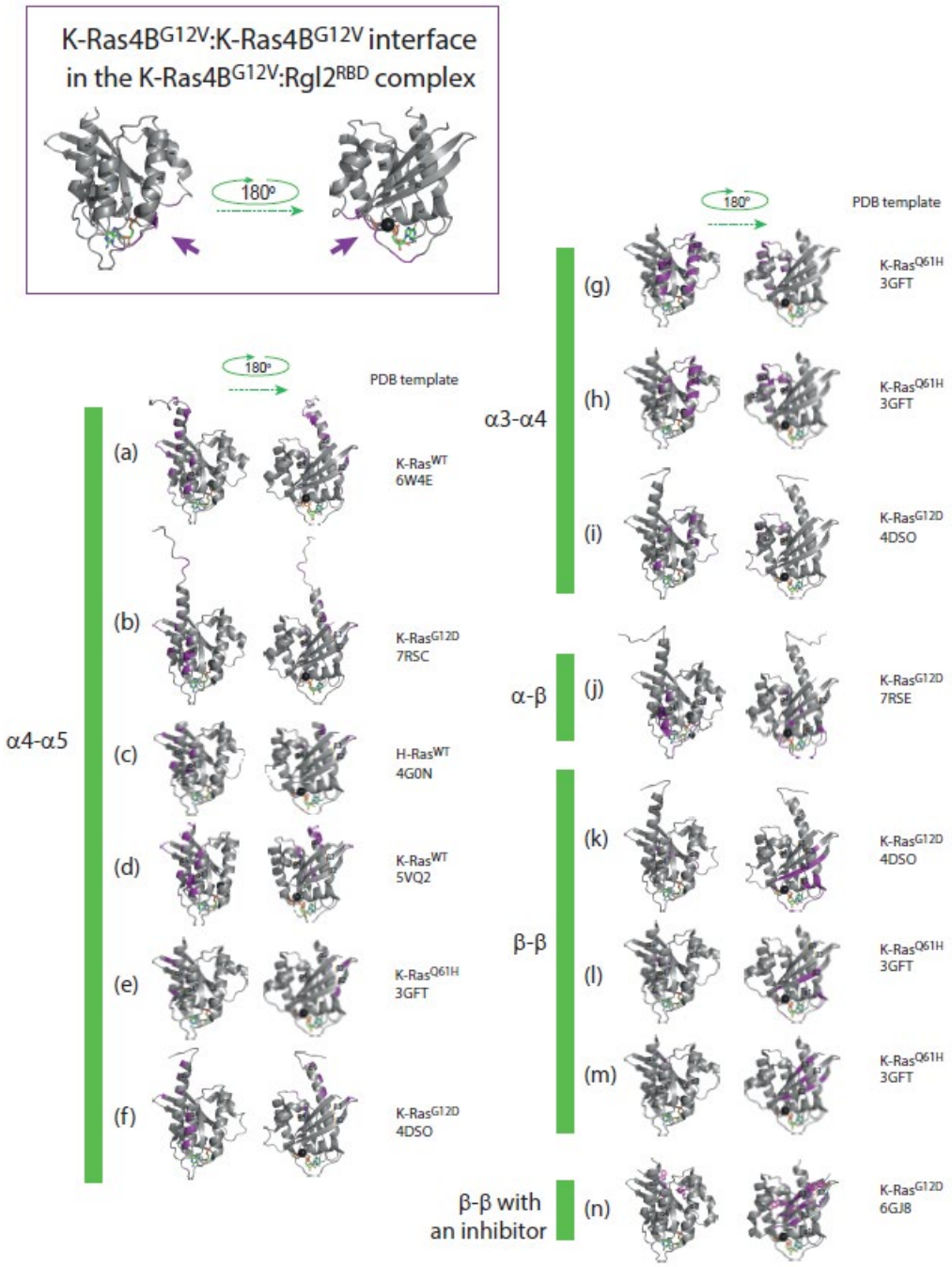

Figure S9. Various Ras:Ras interfaces proposed by experimental and computational prediction studies.

The top panel on the left shows the K-Ras4B^{G12V}:K-Ras4B^{G12V} interface of the K-Ras4B^{G12V}:Rgl2^{RBD} heterotetramer complex (this study). The K-Ras4B^{G12V}:K-Ras4B^{G12V} contacts (shaded in purple) are located in loop regions of Switch-I, Switch-II and α3. The K-Ras4B^{G12V}:K-Ras4B^{G12V} interface is

distinct from previously proposed dimerization interfaces, which can be classified into four categories based on the relevant structural elements; α5-α4, α4-α3, α-β and β-β, as listed in (a)-(n). Images of a single Ras molecule at the Ras:Ras interface are presented with the interacting residues highlighted in purple, and the involved α-helices and β-sheets are annotated. PDB IDs of the image templates are indicated next to each image. **(a)-(f)** Examples of Ras:Ras interfaces that involve α4-α5. **(g)-(i)** Examples of Ras:Ras interfaces that involve α3-α4. **(j)** A K-Ras4B^{G12D}:K-Ras4B^{G12D} interface that lies in α4-β2 and α1-β6. The two K-Ras4B^{G12D} in the dimer are in two different orientations for this interaction to occur. (**k)-(m)** Examples of Ras:Ras interfaces that involve β-β. The interfaces overlap with the effector binding region and are thought to impair effector interaction. **(n)** The dimer formation mediated by the β-β contact was aided by a small molecule inhibitor BI2852 (shown in purple). The Mg^{2+} is depicted as a dark-grey sphere and the bound nucleotide is shown as a ball-and-stick model.

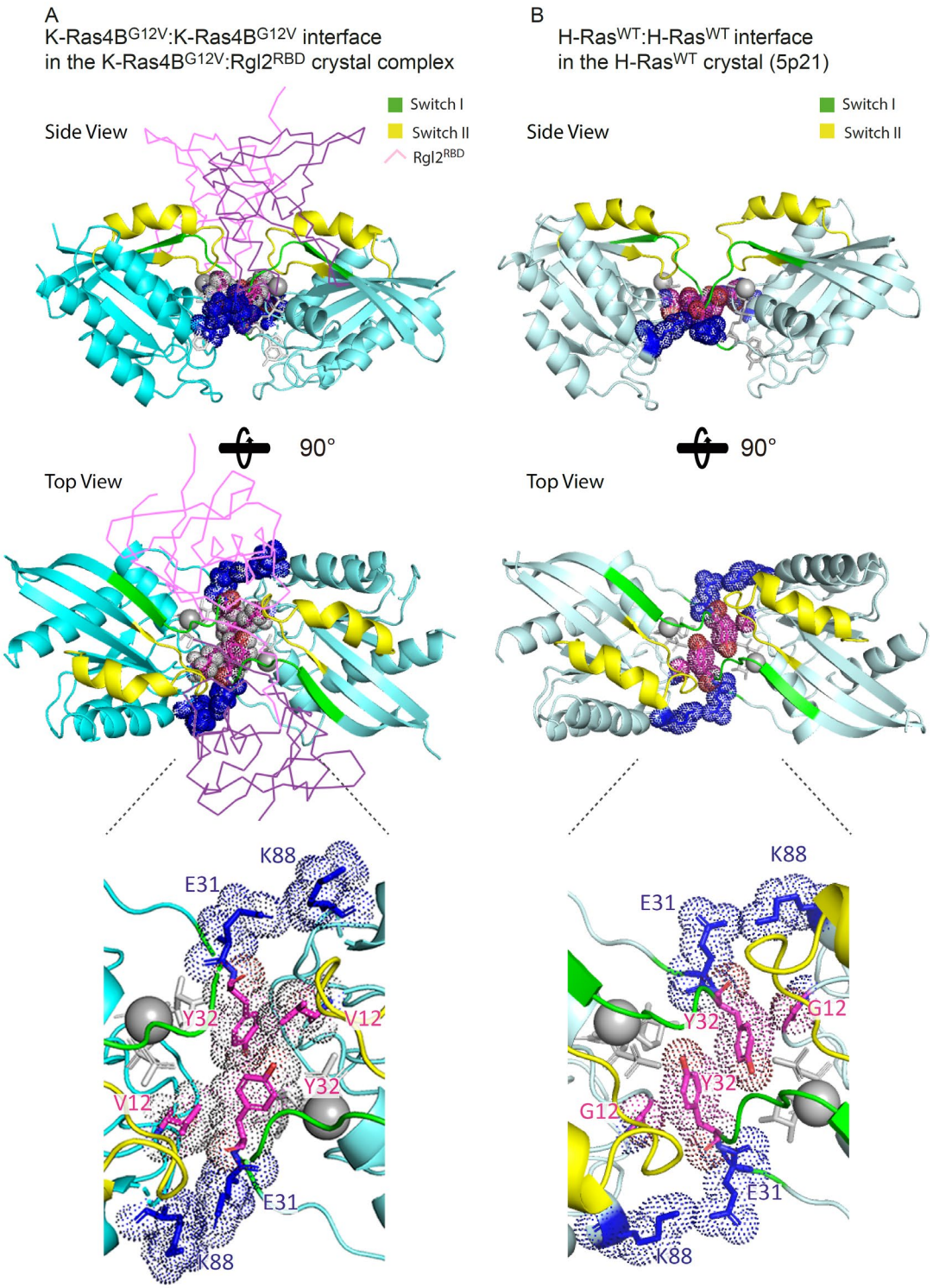

Figure S10. Spatial Ras:Ras arrangements of K-Ras4B^{G12V}:K-Ras4B^{G12V} in the K-Ras4B^{G12V}:Rgl2^{RBD} complex and H-Ras^{WT} crystal structure 5P21

Neighboring Ras molecules are shown to reveal comparable spatial arrangements. The side view (top panel), top view (middle panel) and the blow-up of the area Y32 (bottom panel) are shown. Switch I and Switch II regions are indicated in green and yellow. (A) K-Ras4B^{G12V}:K-Ras4B^{G12V} in the K-Ras4B^{G12V}:Rgl2^{RBD} complex. The Rgl2^{RBD} is shown as a ribbon in light magenta. (B) H-Ras^{WT}:H-Ras^{WT} in the H-Ras^{WT} crystal (5p21). Spatial molecular arrangements around Y32 are similar in both cases, but the oncogenic V12 provides a larger hydrophobic pocket.

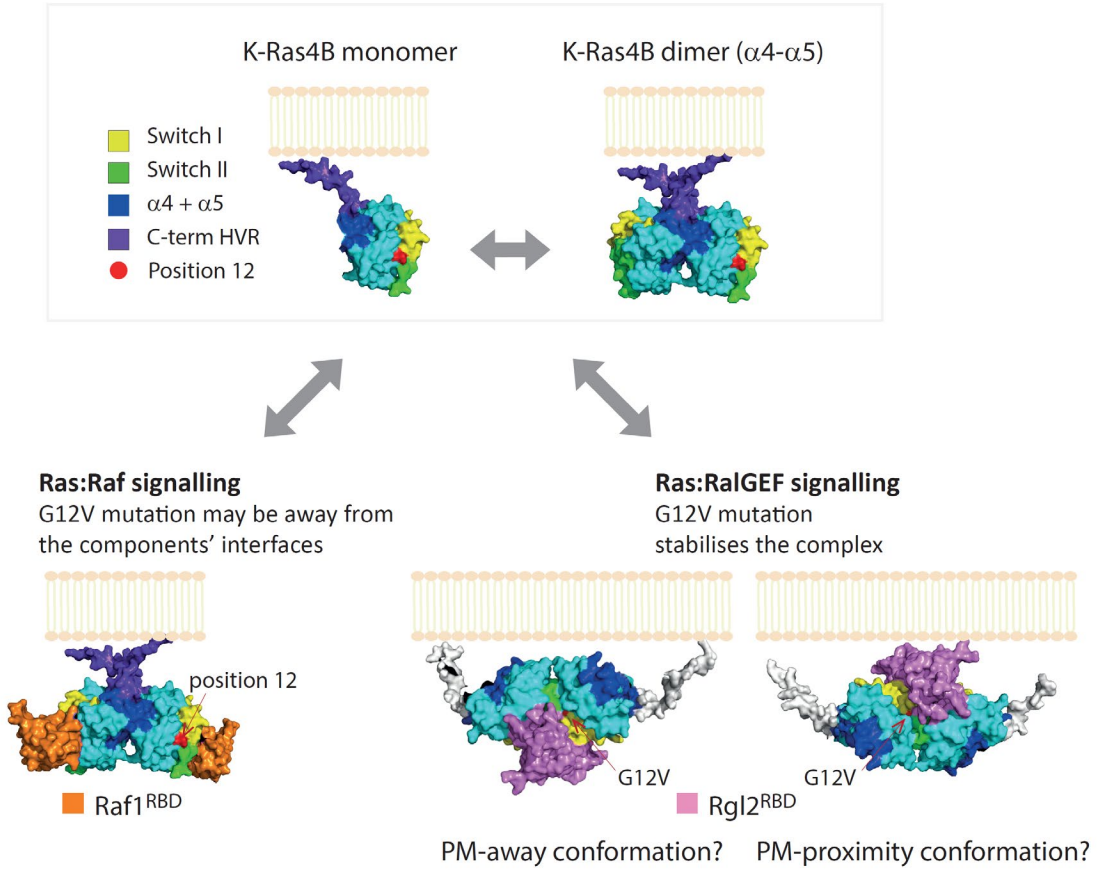

Figure S11. Possible K-Ras4B^{G12V}:Rgl2^{RBD} complex orientations relative to the plasma membrane

Possible conformational arrangements of the K-Ras4B^{G12V}:Rgl2^{RBD} complex at the plasma membrane (PM). The Rgl2^{RBD} molecules may be facing the cytoplasm (PM-away conformation) or the PM (PM-proximity conformation). Cartoons are prepared based on the previously proposed α4-α5 mediated K-Ras4B^{G12D}:K-Ras4B^{G12D} homodimer at the PM (PDB ID 7RSC) (Lee et al., 2021). The Ras:Raf1 kinase heterotetramer cartoon was generated by merging the K-Ras4B^{G12D}:K-Ras4B^{G12D} homodimer (PDB ID 7RSC) and K-Ras4B^{WT}:Raf1 crystal structure (PDB ID 6Vjj) (Tran et al., 2021; Packer et al., 2020). K-Ras4B is depicted in cyan, and domains are colour coded as follows; Switch-I in yellow, Switch-II in green, α4 and α5 helices in blue, C-terminal hypervariable region (HVR) in purple and the residue at position 12 in red. For the K-Ras4B^{G12V}:Rgl2^{RBD} structure, the HVR is in grey, as the K-Ras4B^{G12V} in the original crystal structure lacked the HVR.

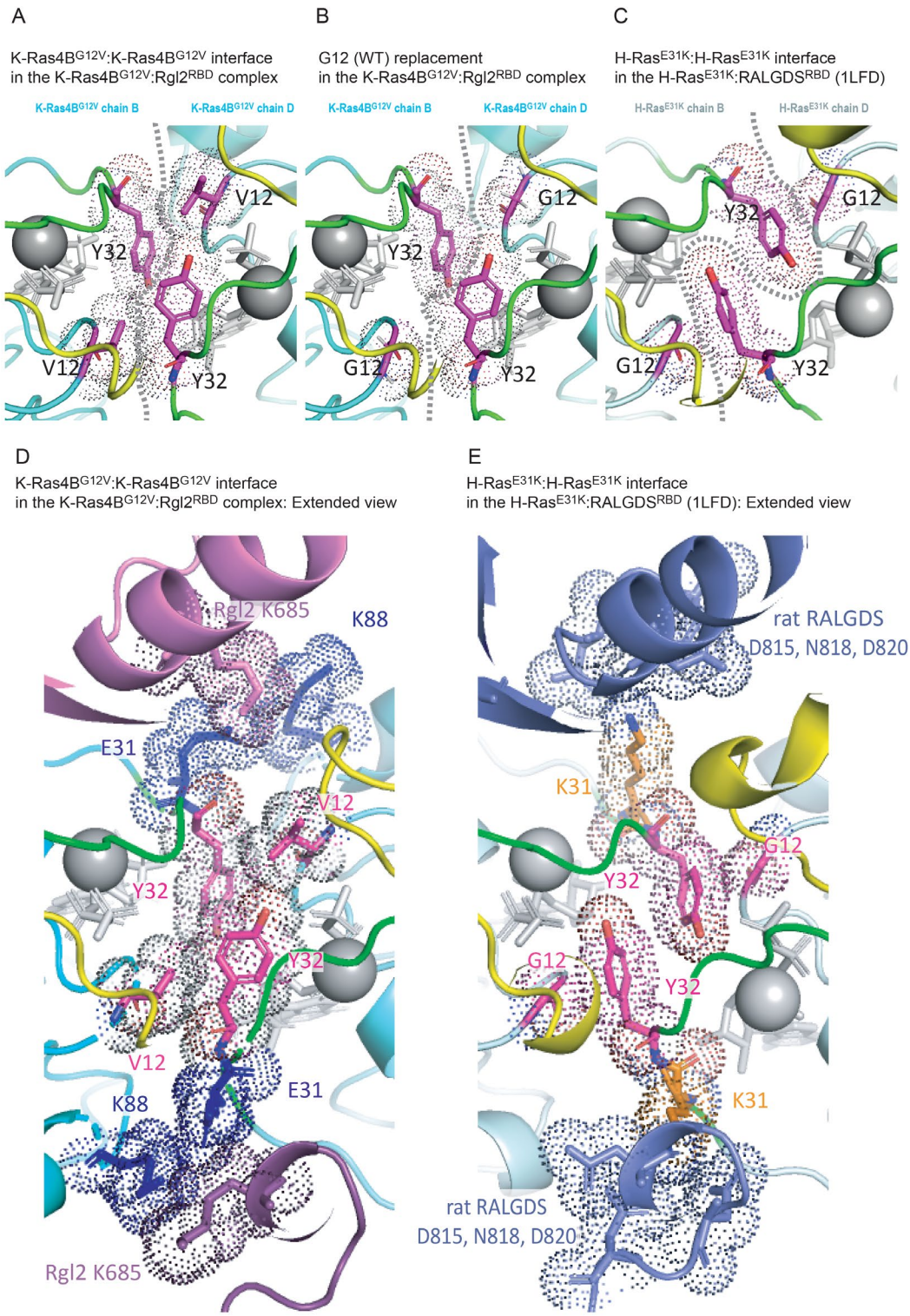

Figure S12. V12 contributes to Ras:Ras interaction

Ras residues at position 12 and Y32 are shown to demonstrate the V12 contribution to stabilise the K-Ras4B^{G12V}:K-Ras4B^{G12V} interface of the K-Ras4B^{G12V}:Rgl2^{RBD} heterotetramer. The Ras:Ras interface is indicated by a grey dotted line in (A)-(C). (A) A cartoon diagram of the K-Ras4B^{G12V}:K-Ras4B^{G12V} interface of the K-Ras4B^{G12V}:Rgl2^{RBD} crystal structure where V12 generates a hydrophobic pocket together with Y32. (B) A simulation of V12 -> G12 replacement in the structure shown in (A). The hydrophobic pocket is reduced by the G12 replacement. (C) A cartoon diagram of the H-Ras^{E31K}:H-Ras^{E31K} interface of H-Ras^{E31K}:RALGDS^{RBD} crystal structure (PDB ID 1LFD). Y32 orientation is different from (A). Nonetheless, with G12, the hydrophobic area around Y32 looks less robust compared to the G12 case shown in (A). (D and E) Extended views of (A) and (C) where the neighbouring E31 (A) and K31 (D) are shown. (D) E31 of K-Ras4B^{G12V} interacts with K-Ras4B^{G12V} K88 and Rgl2^{RBD} K685. (E) The hydrophobic pocket created by Y32 is not reinforced by G12, but K31 of H-Ras^{E31K} interacts with rat RALGDS^{RBD} D815, N818 and D820 (the numbering was done according to Uniprot Q03386), facilitating the complex formation.

Table 1. Data collection and refinement statistics for human K-Ras4B^{G12V}:Rgl2^{RBD} complex. Statistics for the highest-resolution shell are shown in parentheses.

Wavelength	0.9795
Resolution range	28.68 - 3.071 (3.18 - 3.071)
Space group	P 32 2 1
Unit cell	77.843 77.843 163.728 90 90 120
Total reflections	22133 (1819)
Unique reflections	11107 (949)
Multiplicity	2.0 (1.9)
Completeness (%)	98.22 (86.51)
Mean I/sigma(I)	10.15 (2.11)
Wilson B-factor	95.59
R-merge	0.02682 (0.1774)
R-meas	0.03794 (0.2509)
R-pim	0.02682 (0.1774)
CC1/2	0.999 (0.973)
CC*	1 (0.993)
Reflections used in refinement	11065 (936)
Reflections used for R-free	582 (41)
R-work	0.2367 (0.3229)
R-free	0.3204 (0.3572)
CC(work)	0.943 (0.893)
CC(free)	0.849 (0.490)
Number of non-hydrogen atoms	4116
macromolecules	4050
ligands	66
solvent	0
Protein residues	514
RMS(bonds)	0.007
RMS(angles)	1.40
Ramachandran favored (%)	95.22
Ramachandran allowed (%)	3.98
Ramachandran outliers (%)	0.80
Rotamer outliers (%)	0.89
Clashscore	14.47
Average B-factor	113.50
macromolecules	113.74
ligands	98.55

Table 2. NMR structure statistics for Rgl2[a]

Quantity	
Assigned $^{1}H/^{13}C/^{15}N$ chemical shifts	305/256/56
NOE distance restraints[b]	866/281/777
Max. distance restraint violation (Å)	0.13 ± 0.01
Deviations from idealised geometry:	
Bond lengths (Å)	0.0138 ± 0.0001
Bond angles (º)	1.81 ± 0.03
AMBER energy (kcal/mol)	–3624.25 ± 78.09
AMBER vdW energy (kcal/mol)	–279.71 ± 12.49
Ramachandran plot statistics[c] (%)	89.5/10.5/0.1/0
Backbone RMSD (Å)[d]	0.42 ± 0.05
All heavy atom RMSD (Å)[d]	0.84 ± 0.06
Backbone RMSD to the reference (Å)[e]	0.91
All heavy atom RMSD to the reference (Å)[e]	1.68

[a]Where applicable, the average value and the standard deviation over the 20 energy-refined conformers obtained by the program OPALp 2.1 in the presence of the experimental restraints. CYANA calculations were started from 100 conformers with random torsion angle values, simulated annealing with 10,000 torsion angle dynamics steps was applied.
[b]Short/medium/long-range distance restraints derived from NOESY spectra.
[c]Percentage of residues in the most favoured/additionally allowed/generously allowed/disallowed regions of the Ramachandran plot according the program PROCHECK.

[d]RMSD to the mean structure for residues 649-657, and 665–732.

[e]RMSD between the closest structure to the reference among the ensemble conformations and the reference structure (the crystal structure of the K-Ras4B^{G12V}:Rgl2 complex).